

SAND2012-0485
Unlimited Release
Printed January 2012

Final LDRD Report: Metal oxide films, nanostructures, and heterostructures for solar hydrogen production

Coleman X. Kronawitter, Bonnie R. Antoun, Samuel. S. Mao

Prepared by
Sandia National Laboratories
Albuquerque, New Mexico 87185 and Livermore, California 94550

Sandia National Laboratories is a multi-program laboratory managed and operated by Sandia Corporation, a wholly owned subsidiary of Lockheed Martin Corporation, for the U.S. Department of Energy's National Nuclear Security Administration under contract DE-AC04-94AL85000.

Approved for public release; further dissemination unlimited.



Issued by Sandia National Laboratories, operated for the United States Department of Energy by Sandia Corporation.

NOTICE: This report was prepared as an account of work sponsored by an agency of the United States Government. Neither the United States Government, nor any agency thereof, nor any of their employees, nor any of their contractors, subcontractors, or their employees, make any warranty, express or implied, or assume any legal liability or responsibility for the accuracy, completeness, or usefulness of any information, apparatus, product, or process disclosed, or represent that its use would not infringe privately owned rights. Reference herein to any specific commercial product, process, or service by trade name, trademark, manufacturer, or otherwise, does not necessarily constitute or imply its endorsement, recommendation, or favoring by the United States Government, any agency thereof, or any of their contractors or subcontractors. The views and opinions expressed herein do not necessarily state or reflect those of the United States Government, any agency thereof, or any of their contractors.

Printed in the United States of America. This report has been reproduced directly from the best available copy.

Available to DOE and DOE contractors from

U.S. Department of Energy
Office of Scientific and Technical Information
P.O. Box 62
Oak Ridge, TN 37831

Telephone: (865) 576-8401
Facsimile: (865) 576-5728
E-Mail: reports@adonis.osti.gov
Online ordering: <http://www.osti.gov/bridge>

Available to the public from

U.S. Department of Commerce
National Technical Information Service
5285 Port Royal Rd.
Springfield, VA 22161

Telephone: (800) 553-6847
Facsimile: (703) 605-6900
E-Mail: orders@ntis.fedworld.gov
Online order: <http://www.ntis.gov/help/ordermethods.asp?loc=7-4-0#online>



**Final LDRD Report:
Metal oxide films, nanostructures, and heterostructures
for solar hydrogen production**

Coleman X. Kronawitter^{1,2}, Bonnie R. Antoun³, Samuel S. Mao^{1,2}

¹Department of Mechanical
Engineering
University of California,
Berkeley
Berkeley, California 94720

²Environmental Energy
Technologies Division
Lawrence Berkeley National
Laboratory
Berkeley, California 94720

³Mechanics of Materials
Sandia National Laboratories
P.O. Box 969
Livermore, California 94551-0969

Abstract

The distinction between electricity and fuel use in analyses of global power consumption statistics highlights the critical importance of establishing efficient synthesis techniques for solar fuels—those chemicals whose bond energies are obtained through conversion processes driven by solar energy. Photoelectrochemical (PEC) processes show potential for the production of solar fuels because of their demonstrated versatility in facilitating optoelectronic and chemical conversion processes. Tandem PEC-photovoltaic modular configurations for the generation of hydrogen from water and sunlight (solar water splitting) provide an opportunity to develop a low-cost and efficient energy conversion scheme. The critical component in devices of this type is the PEC photoelectrode, which must be optically absorptive, chemically stable, and possess the required electronic band alignment with the electrochemical scale for its charge carriers to have sufficient potential to drive the hydrogen and oxygen evolution reactions. After many decades of investigation, the primary technological obstacle remains the development of photoelectrode structures capable of efficient conversion of light with visible frequencies, which is abundant in the solar spectrum. Metal oxides represent one of the few material classes that can be made photoactive and remain stable to perform the required functions.

This report presents results from research activities in this field performed at the University of California at Berkeley and Lawrence Berkeley National Laboratory by Coleman Kronawitter, awardee of the Excellence in Engineering Fellowship that was established with this LDRD project 151384, Nanostructured Metal Oxide Photoelectrodes for Solar Hydrogen Production. Coleman Kronawitter received his M.S from UC Berkeley in December 2010 and will complete his Ph.D in May 2012.

Acknowledgements

This project was supported by the Laboratory Directed Research and Development program at Sandia National Laboratories, a multiprogram laboratory operated by Sandia Corporation, a Lockheed Martin Company, for the United States Department of Energy under contract DE-AC04-94-AL85000.

Contents

1 Doped, porous iron oxide films and their optical functions and anodic photocurrent for solar water splitting	9
1.1 Abstract for Section 1	9
1.2 Introduction	9
1.3 Optical properties	11
1.4 Summary	14
1.5 References	14
2 Metal oxide hetero-nanostructures for solar water splitting.....	17
2.1 Abstract for Section 2.....	17
2.2 Introduction	17
2.3 Motivation for water oxidation at nanoscale oxide heterostructure photoanodes.....	18
2.3.1 Oxide nanostructures.....	18
2.3.2 Oxide heterostructures	18
2.4 Discussion of selected recent systems.....	20
2.5 Nanoscale architectures.....	20
2.5.1 Bilayers	22
2.5.2 Ultrathin coatings	22
2.6 The α -Fe ₂ O ₃ -WO ₃ system.....	23
2.6.1 Introduction to material system.....	23
2.6.2 Physical and optical characterization	24
2.6.3 Photoelectrochemistry.....	26
2.6.4 Ultrafast transient absorption spectroscopy	29
2.7 Electronic structure of heterostructure interfaces.....	31
2.8 Conclusions	32
2.9 Methods.....	32
2.9.1 Physical characterization.....	33
2.9.2 Photoelectrochemical characterization.....	33
2.9.3 Ultrafast transient absorption spectroscopy	34
2.10 References	34
3 Engineering impurity distributions in photoelectrodes for solar water oxidation.....	41
3.1 Abstract for Section 3.....	41
3.2 Experimental details.....	51
3.3 Supporting information	51
3.3.1 Morphology.....	51
3.3.2 Experimental details.....	52
3.3.3 Ellipsometry-reflectometry	53
3.3.4 Complete IPCE spectra for ZnO:Al-ZnO:Ni system	58
3.3.5 Amperometric (current-time) measurement with color filters for ZnO:Al.....	58
3.4 References	59

4	Electron enrichment in 3d/transition metal oxide hetero-nanostructures	61
4.1	Abstract for Section 4.....	61
4.2	Description of hetero-nanostructure array.....	62
4.3	Ti L-edge x-ray absorption.....	63
4.4	O K-edge x-ray absorption.....	65
4.5	Ti L-edge x-ray emission	67
4.6	O 2p orbital analysis.....	68
4.7	Ultrafast transient absorption spectroscopy	69
4.8	Conclusions	72
4.9	Experimental methods.....	72
4.9.1	Fabrication.....	72
4.9.2	Soft x-ray spectroscopy.....	72
4.9.3	Ultrafast transient absorption spectroscopy	72
4.10	References	73
Appendix: Research Publications.....		77
	International conference presentations	77
	Seminars	77

Figures

Figure 1.	Scanning electron micrographs of films deposited with low and high substrate temperatures	10
Figure 2.	Optical characterization of film deposited on SiO ₂ at 300 °C:.....	12
Figure 3.	Photoelectrochemical performance in 0.1 M NaOH aqueous electrolyte (pH=13)	13
Figure 4.	Illustrations depicting the primary processes responsible for performance enhancements in oxide heterostructure photoelectrodes.	19
Figure 5.	Illustration depicting the design of metal oxide hetero-nanostructure arrays and their application as photoanodes for photoelectrochemical cells.....	24
Figure 6.	(a) SEM images of α -Fe ₂ O ₃ arrays as fabricated by aqueous chemical growth.	25
Figure 7.	Photoelectrochemical characterization in aqueous 0.5 M NaCl solution.....	27
Figure 8.	Ultrafast transient absorption spectroscopy for hetero-nanostructure electrodes.....	30
Figure 9.	Scanning electron microscopy images of ZnO nanostructure arrays, with yellow arrows highlighting doped crystallites distributed approximately 1.5 μ m along the direction of light propagation.	43
Figure 10.	Structural and optical characterization of ZnO nanostructure arrays with and without ZnO:Ni modification.....	44
Figure 11.	Photoelectrochemical characterization of ZnO electrodes in 0.5 M Na ₂ SO ₄	46
Figure 12.	Idealized energetics of the functional homojunction nanostructures demonstrated in this study.....	48

Figure 13. Light harvesting efficiency (top panel) and absorbed photon conversion efficiency (bottom panel) as defined in the main text.	49
Figure 14. Top-down SEM images of ZnO nanorod arrays before (a) and after (b) modification with ZnO:Ni. White scale bars indicate 2.5 μm	51
Figure 15. (a) Experimental (Exp) and simulated (Sim) values for reflection measured at normal incidence and ellipsometric parameters ψ and Δ measured at 70° incidence. (b) Multi-layer structure employed for simulation of ellipsometry-reflectometry data, with thickness and composition quantities determined by the regression analysis. (c) Cross-section SEM image of the ZnO/Si structure. White scale bar indicates 500 nm.	55
Figure 16. (a) Complex dielectric function, $\epsilon_1 + i\epsilon_2$, as determined by ellipsometry-reflectometry regression analysis. (b) Spectral absorption coefficient and its reciprocal, the mean light penetration depth, for a ZnO:Ni thin film.	57
Figure 17. Complete spectra for incident photon conversion efficiencies for front-side irradiation of ZnO:Al – ZnO:Ni photoelectrodes, as described in the main text, in 0.5 M Na_2SO_4 with +1 V applied versus a Pt counter electrode.	58
Figure 18. Amperometric current-time measurement for ZnO:Al with chopped AM 1.5G-filtered 100 mW cm^{-2} irradiation at 0.6 V vs Ag/AgCl, with application of color filters.	58
Figure 19. Transmission electron microscopy image of the $\text{Ti}_x\text{O}_y\text{-Fe}_2\text{O}_3$ hetero-nanostructure interface, with lattice fringes evident. Inset provides a lower resolution image of the tip of a complete structure.	63
Figure 20. Ti $L_{\text{II,III}}$ -edge x-ray absorption spectra for $\text{Ti}_x\text{O}_y\text{-Fe}_2\text{O}_3$ and reference TiO (red), Ti_2O_3 (black), and TiO_2 (brown)	64
Figure 21. (a) O K_α -edge x-ray absorption spectra for $\text{Ti}_x\text{O}_y\text{-Fe}_2\text{O}_3$ and reference crystals.	66
Figure 22. Ti $L_{\text{II,III}}$ -edge x-ray emission spectra for $\text{Ti}_x\text{O}_y\text{-Fe}_2\text{O}_3$ and reference titania crystals with indicated electronic configurations.	68
Figure 23. Combined O $1s$ x-ray emission and absorption spectra for $\text{Ti}_x\text{O}_y\text{-Fe}_2\text{O}_3$, with the first derivatives for each spectrum included for quantification of the energy difference between occupied and unoccupied p projected density of states.	69
Figure 24. (a) Transient absorbance spectra before (black circles) and 500 fs (blue squares) after excitation. Normalized transient absorption signals for four representative probe wavelengths at ~ 1 ps (b) and ~ 10 ps (c) time regimes. (d) Transient absorption (averages of signals from 70 to 100 ps) after ultrafast excitation of $\text{Ti}_x\text{O}_y\text{-Fe}_2\text{O}_3$ array at various probe wavelengths (blue squares).	70

Tables

Table 1. Summary of selected recent oxide heterostructure systems discussed in this report.	22
Table 2. Values for Cauchy relations used for simulation of SiO ₂	56
Table 3. Fitted values for Tauc-Lorentz parameterization and associated standard errors.....	56

1 Doped, porous iron oxide films and their optical functions and anodic photocurrent for solar water splitting

1.1 Abstract for Section 1

The fabrication and morphological, optical, and photoelectrochemical characterization of doped iron oxide films is presented. The complex index of refraction and absorption coefficient of polycrystalline films are determined through measurement and modeling of spectral transmission and reflection data using appropriate dispersion relations. Photoelectrochemical characterization for water photo-oxidation reveals that the conversion efficiencies of electrodes are strongly influenced by substrate temperature during their oblique-angle physical vapor deposition. These results are discussed in terms of the films' morphological features and the known optoelectronic limitations of iron oxide films for application in solar water splitting devices.

Alpha-phase iron(III) oxide (hematite, $\alpha\text{-Fe}_2\text{O}_3$) is an earth-abundant transition metal oxide compound that possesses many of the requisite characteristics for employment in efficient and scalable solar energy conversion technologies. It is inexpensive, non-toxic to humans, absorbs ultraviolet and high energy visible light, is electrochemically stable in a wide range of conditions, and its valence band edge is appropriately positioned to accept charges for the oxidation of water. It can function as a photoactive electrode material in photoelectrochemical (PEC) cells for solar energy conversion, most notably several promising tandem designs for solar hydrogen generation.^{1,2} Its implementation into solar energy conversion devices presents some interesting technical challenges, mainly associated with its notoriously poor electronic transport properties (e.g. $\mu_{\text{electron}} < 0.1 \text{ cm}^2 \text{ V}^{-1} \text{ s}^{-1}$ ³; $l_{\text{diffusion, hole}} \sim 2\text{-}4 \text{ nm}$ ⁴). Consequently the general strategy employed toward fabrication of efficient $\alpha\text{-Fe}_2\text{O}_3$ photoelectrodes has been to simultaneously dope the lattice and to reduce the physical dimensions of the electrode structure to more nearly match the hole diffusion length. These efforts have been fruitful and yield very promising results; research into doped, nanostructured $\alpha\text{-Fe}_2\text{O}_3$ water splitting photoanodes has recently been comprehensively examined in Reference 5.

1.2 Introduction

One possible fabrication route to structures of this type is their oblique-angle or glancing-angle physical vapor deposition, the benefits of which have been established in the literature⁶. These techniques have been explored recently for photoelectrochemical and photocatalytic applications of TiO_2 ,⁷ $\alpha\text{-Fe}_2\text{O}_3$,⁸ ZnO ,⁹ WO_3 ,¹⁰ and composites thereof,¹¹ all of which are important solar water splitting materials. The typical motivation behind the unconventional geometry is the utilization of film growth shadowing phenomena resulting from ballistic species transport to the substrate, which can affect a nanostructured morphology. Engineering films by this technique is therefore particularly relevant to the study of iron oxide-based photoelectrodes because it enables fabrication of films with the aforementioned required physical properties (appropriate chemical composition and nanoscale morphology). This work is intended to contribute to the growing

literature dedicated to the study of α -Fe₂O₃-based photoelectrodes for solar energy conversion, as well as to that of the oblique angle physical vapor deposition of metal oxides in general.

In this study, films were deposited onto conductive SnO₂:F-coated glass (FTO) and SiO₂ substrates in an oxygen environment at a moderate vacuum pressure of 4 mtorr. Deposition occurred from species ablated from a Fe₂O₃:TiO₂ (2.5 wt% TiO₂) target by approximately 130,000 shots from an excimer laser (Lambda Physik), with a laser fluence of $\sim 1\text{mJ}/\text{cm}^2$ on the target surface. Although the exact nature of resulting Ti incorporation into the films' crystal lattice was not studied, film composition analysis by x-ray fluorescence (50 kV Cu K α radiation, Xradia) indicates the Ti content in the films is 2.25 atomic percent. The substrate was positioned at an angle of 49° from the target normal.¹² The importance temperature-related effects for this material system has been noted in the literature,¹³ consequently three deposition substrate temperatures were examined (23 °C, 100 °C, 300 °C), and all samples were subsequently heat treated in air at 450 °C for 2 hrs before characterization. Adatom surface diffusion is an activated process and depends exponentially on temperature¹⁴ – it is expected that depositions employing low substrate temperatures produce porous films with little structural organization, while those using high temperatures produce dense films with greater structural quality. Scanning electron microscopy images in Figure 1a,c of a sample deposited at 300 °C confirm that when species arriving at the substrate possess sufficient thermal energy for diffusion, a dense, rough, polycrystalline sample is produced. When the substrate is kept at 23 °C surface diffusion is quenched and a nanostructured (porous) morphology is attainable (Figure 1b,d).¹² Films deposited at 100 °C appeared in micrographs to have an intermediate level of porosity (not shown). The cross-sectional views indicate the films develop through the columnar growth mode,¹⁴ which is expected to minimize the density of grain boundaries along the electronic conduction path normal to the substrate.

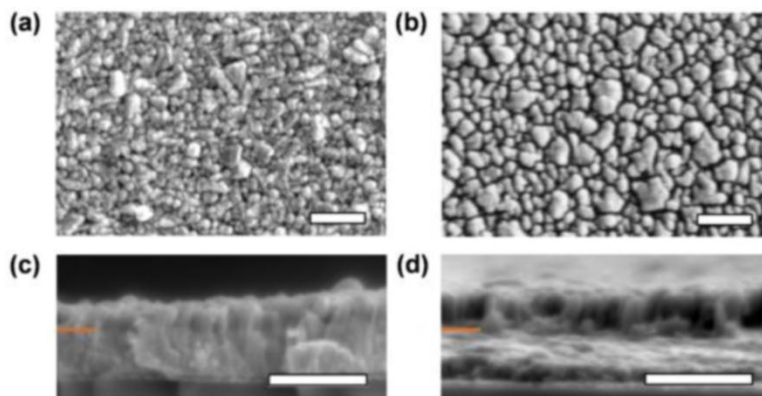


Figure 1. Scanning electron micrographs of films deposited with low and high substrate temperatures: (a) top-down view of 300 °C sample; (b) cross-sectional view of 300 °C sample; (c) top-down view of 23 °C sample; (d) tilted cross-sectional view of 23 °C sample. All white scale bars indicate 1 μm . Orange lines highlight film/substrate interfaces.

1.3 Optical properties

The optical properties of films were analyzed by measurement and subsequent modeling of spectral normal transmission and 0 (normal) and 70 degree specular reflection data using a thin film metrology system and its multi-layer film analysis software (FilmTek 3000 PAR SE). During deposition a small 0.5 mm thick single crystal SiO₂ substrate was mounted onto the FTO substrate surface at a location approximately 1 cm from the area later probed by PEC measurements. The measured quantities for the 300 °C sample are presented in 2a. The sample was modeled as a three layer substrate/film/surface roughness structure as shown Figure 2b, and a regression analysis was performed utilizing the Cauchy dispersion¹⁵ for the substrate, the Tauc-Lorentz dispersion relation¹⁶ for the film, and the Bruggeman¹⁷ EMA relation for surface roughness (modeled values indicated by lines in Figure 2a).¹² This analysis yielded a correlation coefficient of $R^2 = 0.995$ and predicts a film thickness of 303.5 nm and a surface roughness thickness of 34.7 nm, which is consistent with the microscopy image in Figure 1c. The resultant modeled optical data correspond to the complex index of refraction displayed in Figure 2c. These index magnitudes are relatively consistent with previous estimates for those of Fe₂O₃:Ti¹⁸ and reflect the known optical transitions of α -Fe₂O₃ between 1.9 eV to 2.2 eV. Figure 2d presents the absorption coefficient as calculated from the extinction coefficient in Figure 2c; these values suggest that several hundred nanometers of material are required for complete optical absorption of longer wavelength light. The disparity between this quantity and the minority carrier diffusion length in α -Fe₂O₃ is the primary obstacle for its technological implementation in PEC cells for solar energy conversion. Similar analyses of several locations on the FTO substrate indicate that over the 1 cm² probed by PEC measurements, the thickness gradient does not exceed ~20 nm/cm.

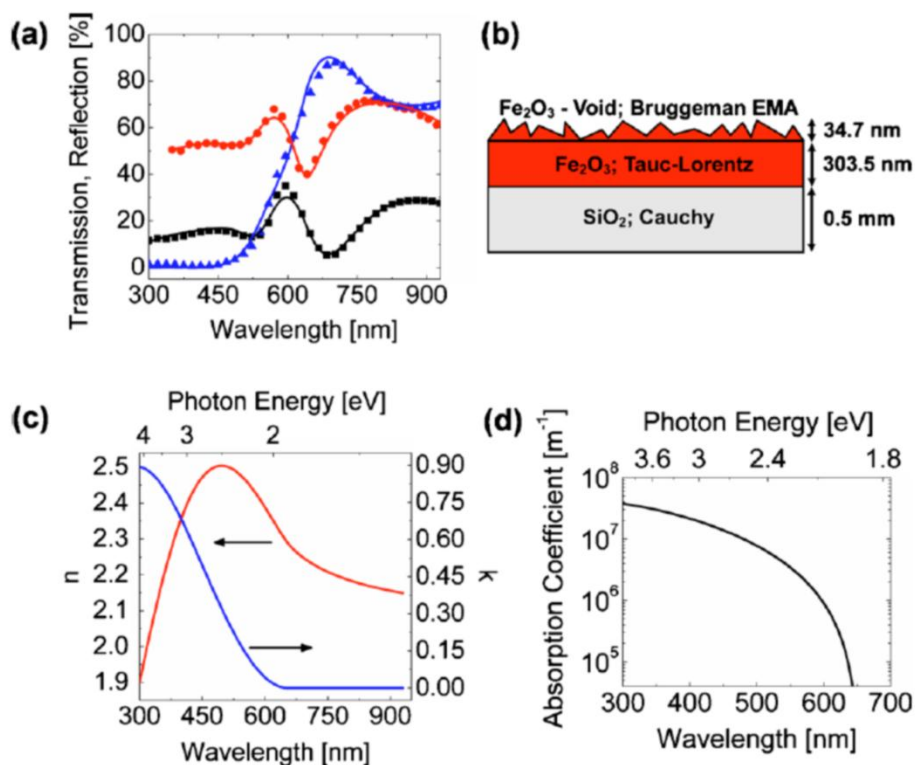


Figure 2. Optical characterization of film deposited on SiO₂ at 300 °C: (a) measured spectral normal transmission (blue triangles), 0° reflection (black squares), and 70° reflection (red circles). Every fortieth data point plotted for clarity. Simulated values are indicated by overlapping solid lines. (b) Multi-layer structure used as model for simulation of optical functions, with final determined values for layer thickness included. (c) Complex index of refraction $\tilde{n} = n + ik$ corresponding to the model presented in (a). (d) Absorption coefficient as calculated from the extinction coefficient in (c).

Photocurrent-potential curves (linear sweep voltammograms) for films employed as working electrodes in a three electrode PEC cell fitted with a quartz window are shown in Figure 3a (Xe lamp solar-simulated light, Newport). There is a striking increase of anodic photocurrent magnitude with increasing substrate deposition temperature. The photocurrent magnitudes are more clearly indicated by the amperometric current-time curves displayed in Figure 3b, which show over an order of magnitude photocurrent range among the samples. The spectral characteristics of these trends are shown in Figure 3c with two-electrode incident photon conversion efficiency (IPCE) data, obtained with the use of a monochromator (5 nm FWHM bandwidth, 10 nm interval) and measurement of photon flux with a NIST-calibrated silicon photodiode. These data are compared in Figure 3c to the spectral absorptance, calculated from the absorption coefficient and film thickness as indicated in the right axis label. The discussion that follows elaborates upon the relationships among these quantities.

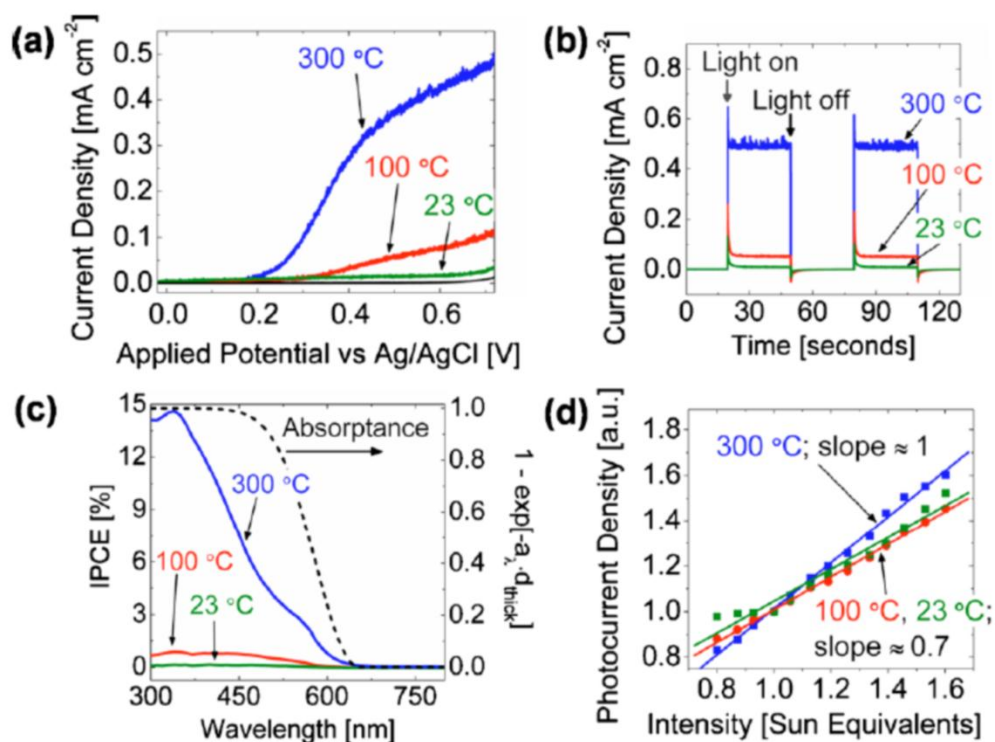


Figure 3. Photoelectrochemical performance in 0.1 M NaOH aqueous electrolyte (pH=13) (a) Photocurrent-potential curves for samples deposited at 23 °C (green line), 100 °C (red line), and 300 °C (blue line) irradiated on the back side by 100 mW cm⁻², AM 1.5 G-filtered solarsimulated light. (b) Current-time curves at 0.6 V vs Ag/AgCl with the same optical conditions as (a) but irradiated on the front side. (c) Incident photon conversion efficiency for front-side irradiation in two-electrode setup with an applied bias of +1 V vs counter electrode, plotted with absorption coefficient of 300 °C sample. (d) Photocurrent data collected at 0.6 V vs Ag/AgCl for 13 irradiation intensities with linear interpolations among data as described in the main text.

Examination of the temperature-photocurrent-irradiation intensity relationships for the samples provides additional information. Figure 3d shows the photocurrent density-intensity dependence of samples normalized by their respective photocurrents at 1 sun-equivalent irradiation. Linear interpolations are provided because the production of free electrons is directly proportional to light intensity.¹⁹ The slopes of linear fits ($R^2 > 0.958$) to these data (1.01 ± 0.02 for 300 °C, 0.72 ± 0.01 for 100 °C, and 0.70 ± 0.04 for 23 °C) are a measure of the efficiencies with which the structures are able to convert additional photon flux into current density in the external circuit. The initial interpretation of this photocurrent-deposition temperature dependence acknowledges the poor electronic transport properties of n-type α -Fe₂O₃.⁴ In the analysis that follows, it is assumed that the surface properties and consequently kinetics for water oxidation among the films are identical. This assumption seems reasonable considering their near-identical fabrication procedure and materials. The function of an n-type photoanode in a cell of this type is 5 to generate and transport to the semiconductor-electrolyte interface holes with sufficient electrochemical potential to drive the oxygen evolution reaction. Electrons must be transported

to the back contact where they enter the external circuit to participate in an electrochemical reduction reaction (e.g. proton reduction for H₂ generation). Considering that the reciprocal of the absorption coefficient (Figure 2d) is equal to the mean light penetration depth in a homogeneous system, this spectral quantity provides a measure of the average depth in the film up to which electron-hole pairs are created. The importance of this relationship is reflected in the spectral absorbance shown in Figure 3c, which indicates that although the films are optically thick at wavelengths below ca. 500 nm, the IPCE values remain low in this spectral range and gradually decrease with increasing wavelength. Electron conduction in α -Fe₂O₃ occurs in narrow Fe d levels³ and has been described to occur by the small polaron hopping mechanism.²⁰ Consequently charge transport in this material is especially sensitive to defect concentrations. It is observed that in the lower energy region, where the longer light penetration depth requires longer carrier transport distances, lower photocurrents are measured in the external circuit. It could be inferred that although low temperature samples likely possess a higher degree of porosity and therefore greater electrochemically active surface area (see Figure 1b,d), the high temperature sample's expected superior transport properties outweigh this advantage.

The photocurrent-intensity dependencies in Figure 3d confirm the existence of differing transport properties among the films. Slopes near unity in plots of this type, as observed for the 300 °C sample, have been previously measured in conditions where electron-hole recombination is not significant.²¹ The slope associated with the low temperature samples, near 0.7, indicates that even over the weak intensity range studied (80-160 mW cm⁻²), these films are unable to efficiently convert additional photon flux into photocurrent. Most probably significant electron-hole recombination would be observed in the form of non-linear current-intensity dependences for all samples at irradiation intensities higher than those permitted within the experimental constraints of the present study. The comparatively weaker current-intensity dependence even at low intensities for samples deposited at low temperatures suggests severe transport limitations in these structures, perhaps originating from lattice disorder or higher densities of surface trap states caused by their apparently higher surface area.

1.4 Summary

This section presented the morphological, optical, and photoelectrochemical characterization of doped iron oxide film electrodes for implementation into solar water splitting PEC devices. It was determined that despite their apparent increased surface area, porous electrodes deposited at 23 °C were significantly less efficient than denser electrodes deposited at 300 °C. It is hoped that such a finding is applicable to future studies of the fabrication of efficient iron-oxide-based photoanodes, which is known to require careful film growth engineering. In attempting to fabricate nanostructured Fe₂O₃ films for this application great care must be taken to maintain the structural quality and related electronic character of crystallites.

1.5 References

1. J. Augustynski G. Calzaferri, J. Courvoisier, and M. Grätzel, in Proceedings of the 11th World Hydrogen Energy Conference, edited by T. N. Veziroglu, C.- J. Winter, J. P. Baselt, and G. Kreysa (DECHEMA, Frankfurt, 1996), p. 2378.

2. E. L. Miller, R. E. Rocheleau, and X. M. Deng, *Int. J. Hydrogen Energy* 28, 615 (2003).
3. F. J. Morin, *Phys. Rev.* 93, 1195 (1954).
4. J. H. Kennedy and K. W. Frese, *J. Electrochem. Soc.* 125, 709 (1978).
5. V. R. Satsangi, S. Dass, and R. Shrivastav, in *On Solar Hydrogen and Nanotechnology*, edited by L. Vayssieres (Wiley, Singapore, 2009), pp. 349–397.
6. K. Robbie, J. C. Sit, and M. J. Brett, *J. Vac. Sci. Technol. B* 16, 1115 (1998).
7. A. Wolcott, W. A. Smith, T. R. Kuykendall, Y. Zhao, and J. Z. Zhang, *Small* 5, 104 (2009).
8. N. T. Hahn, H. Ye, D. W. Flaherty, A. J. Bard, and C. B. Mullins, *ACS Nano* 4, 1977 (2010).
9. A. Wolcott, W. A. Smith, T. R. Kuykendall, Y. Zhao, and J. Z. Zhang, *Adv. Funct. Mater.* 19, 1849 (2009).
10. W. Smith, Z. Y. Zhang, and Y. P. Zhao, *J. Vac. Sci. Technol. B* 25, 1875 (2007).
11. W. Smith and Y. P. Zhao, *Catal. Commun.* 10, 1117 (2009).
12. K. Sivula, R. Zboril, F. Le Formal, R. Robert, A. Weidenkaff, J. Tucek, J. Frydrych, and M. Grätzel, *J. Am. Chem. Soc.* 132, 7436 (2010).
13. D. L. Smith, *Thin-Film Deposition: Principles and Practice* (McGraw-Hill, Boston, 1995).
14. H. Fujiwara, *Spectroscopic Ellipsometry: Principles and Applications* (Wiley, West Sussex, 2007).
15. G. E. Jellison and F. A. Modine, *Appl. Phys. Lett.* 69, 371 (1996).
16. D. A. G. Bruggeman, *Ann. Phys.* 416, 636 (1935).
17. J. A. Glasscock, P. R. F. Barnes, I. C. Plumb, and N. Savvides, *J. Phys. Chem. C* 111, 16477 (2007).
18. M. D. Ward, J. R. White, and A. J. Bard, *J. Am. Chem. Soc.* 105, 27 (1983).
19. K. M. Rosso, D. M. A. Smith, and M. Dupuis, *J. Chem. Phys.* 118, 6455 (2003).
20. H. Wang, T. Lindgren, J. He, A. Hagfeldt, and S. -E. Lindquist, *J. Phys. Chem. B* 104, 5686 (2000).

This page intentionally left blank.

2 Metal oxide hetero-nanostructures for solar water splitting

2.1 Abstract for Section 2

A study of the design of all-oxide heterostructures for application in photoelectrochemical cells for solar water splitting is provided. Particular attention is paid to those structures which possess nanoscale feature dimensionality, as structures of this type are most likely to utilize the benefits afforded by the formation of oxide heterojunctions and likely to show functional behavior relating to the interfacial region. In the context of this discussion, a novel hetero-nanostructure array, based on quantum-confined and visible light-active iron(III) oxide nanostructures and their surface modification with tungsten(VI) oxide, is introduced. The heterostructure architecture is designed to combine the functionality of the constituent phases to address the primary requirements for electrodes enabling the efficient generation of hydrogen using solar energy: visible light activity, chemical stability, appropriate band edge characteristics, and potential for low-cost fabrication. Photoelectrochemical characterization for solar hydrogen/oxygen generation indicates the presence of unexpected minority carrier transfer dynamics within the oxide hetero-nanostructures, as observed additionally by ultrafast transient absorption spectroscopy.

This work involved some measurements from collaboration with researchers at University of California at Santa Cruz. Specifically it involved collaboration with Damon Wheeler and Jin Zhang in the UC Santa Cruz Department of Chemistry and Biochemistry.

2.2 Introduction

Metal oxide heterostructures can be engineered to possess functional behavior that results both from the bulk properties of their constituent phases as well as from the emergent properties that relate directly to the electronic and atomic character of their interfaces. The study of oxide heterostructures has led to the discovery of a number of new and technologically promising interfacial phenomena, including magnetism from non-magnetic materials,¹ electronic conductivity from insulators,² and emergent ionic conductivity.³

In addition to their prospective application as electronic and magnetic device components, oxide heterostructures have been applied as photoactive components of photoelectrochemical (PEC) devices devoted to the clean and sustainable generation of hydrogen from water using sunlight. The motivation for these applications relates to diversity of cation oxidation states, crystal structures, and electronic configurations, and to the concomitant material properties, associated with oxides and especially with the oxides of the transition metals. Utilizing this diversity by combining dissimilar oxide materials allows for design of photoelectrodes specialized to perform the optical, electronic, and chemical functions required of PEC solar water splitting cells.

This perspective focuses on the design of all-oxide heterostructure photoanodes whose function is to enable the photo-oxidation of water, a critical and performance-limiting half reaction in the overall splitting of water to produce hydrogen and oxygen gas.⁴ Particular attention is paid to

those heterostructures with nanoscale dimensionality, as structures of this type are most likely to utilize the benefits afforded by the formation of oxide heterojunctions and likely to show functional behavior relating to the interfacial region. For detailed analyses of alternative designs, readers are referred to the comprehensive and ever-expanding literature of this field, which most recently includes books,⁵ general and comprehensive reviews,^{6,7} including progress in α -Fe₂O₃ electrodes,^{8,9} discussions of composite systems incorporating catalytic phases,¹⁰ and summaries of the use of nanomaterials,¹¹ among others.

2.3 Motivation for water oxidation at nanoscale oxide heterostructure photoanodes

2.3.1 Oxide nanostructures

The in-depth consideration of physical processes that occur on nanometer length scales is the defining principle guiding advances in the next generation of solar energy conversion technologies.¹² The application of nanoscience to solar energy conversion appears to represent a pivotal step toward implementing cost-effective energy conversion schemes.^{5,6,13,14,15,16,17} Recent notable contributions in this area include the in-depth study of Si nanowire arrays for photovoltaics^{18,19} the fabrication of efficient dendritic α -Fe₂O₃ nanostructures for water oxidation,⁸ and the use of plasmonic resonance modes to enhance PEC performance.²⁰ Most important to the success of these endeavors is the design of new materials, structures, or architectures that can utilize a fast-growing understanding of nanoscale optoelectronic phenomena, and which can potentially bypass or surpass certain constraints that arise from consideration of conventional materials for this application.

Metal oxide nanomaterials in particular have been extensively investigated for application to solar energy conversion for their diversity of optical properties, electronic and ionic transport properties, chemical and thermal stability, ease of fabrication, and relative low cost. When integrated into solar energy conversion devices, single-crystalline one-dimensional (1-D) metal oxide structures optimize crucial operation processes by increasing optical path lengths and providing direct electronic carrier transport pathways. Aligned oxide nanostructures can now be fabricated onto large-area substrates using controllable and inexpensive techniques.²¹

Photoactive oxide nanomaterials – those with suitable bandgaps to absorb visible light – are stable when irradiated and biased in most chemical environments, and are therefore compatible with a number of PEC device configurations for solar electricity and renewable fuel production. This includes semiconductor-based PEC cells for water splitting or electricity generation²² as well as dye-²³ and quantum dot-sensitized¹² solar cells. However, no single photoactive metal oxide material has proven to possess the required optoelectronic properties to efficiently convert solar light energy into electrical or chemical energy; although recent promising results indicate progress in this direction.²⁴

2.3.2 Oxide heterostructures

A summary of the various motivations for design of oxide heterostructures for solar water oxidation is presented in Figure 4. As has been established in the decades of research in tandem

photovoltaics, placing in series multiple optical absorbers has the potential to dramatically increase the overall conversion efficiencies of solar energy conversion devices. Because of the known thermodynamic requirements⁷ for the photo-oxidation of water, it is likely a successful heterostructure will involve successive absorption of UV and visible (blue, green, and yellow) light.

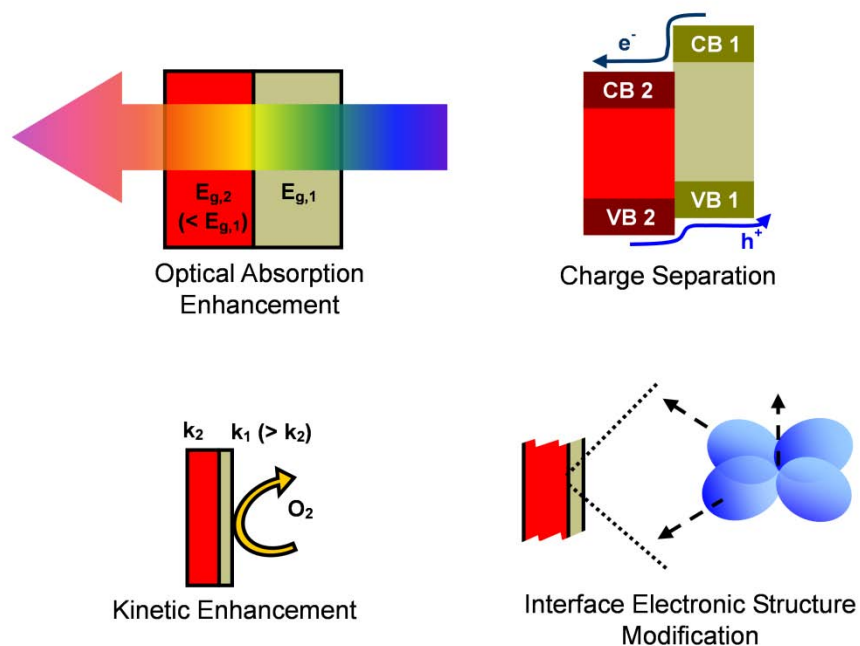


Figure 4. Illustrations depicting the primary processes responsible for performance enhancements in oxide heterostructure photoelectrodes.

Optical absorption enhancements effected by multiple bandgaps translate to conversion efficiency enhancements only if the band structure alignments permit efficient utilization of photoexcited charges. In solid-state nanostructured photovoltaic devices, heterostructures comprised of photoactive semiconductors exhibiting Type II band offsets are utilized to promote the efficient separation of photogenerated charges under irradiation.²⁵ Similarly, in dye- and quantum dot-sensitized solar cells, heterojunctions of transparent oxides with differing electron affinities are utilized to suppress detrimental back reactions (or charge recombination). By directing charges to lower energy states physically separated from the photoexcited dye or quantum dots, this technique has led to efficiency enhancements in both nanoparticulate²⁶ and nanorod²⁷ configurations.

Band offsets among photoactive oxides can promote charge separation if the constituent phases and their junctions provide the necessary conduction pathways for efficient operation of the electrochemical cell. Establishing efficient conduction paths in oxide heterostructure photoanodes is complicated generally by the orbital composition of most relevant oxides' occupied electronic structures: valence band edges are primarily of O $2p$ character, resulting in

little deviation in ionization potential among the oxides.²⁸ Their common orbital character creates difficulty in establishing valence band offsets that facilitate hole separation during operation of the oxide heterostructure photoanode. However, because the oxides' conduction bands are generally cationic in character,²⁸ this observation contrasts with that found for electron transfer across heterojunctions. The recent development of highly efficient Cu₂O-based heterostructure photocathodes²⁹ highlights the additional versatility provided by energy bands whose chemical character is primarily cationic.

There is considerable evidence available suggesting that the surface modification of oxide photoanodes with ultrathin oxide coatings has the potential to affect enhanced kinetics for water oxidation at the oxide-electrolyte interface. Ultrathin coatings permit electron tunneling, passivate dangling bonds, or possess electronic structures that differ from corresponding bulk structures. These configurations potentially alleviate restrictions associated with incompatible band alignments.

Finally, it is suggested here that the fabrication of oxide hetero-nanostructures possessing high interfacial areas is likely to enable the development of materials with entirely new electronic structures, with associated electronic and optical properties and thus technological potential. As will be elaborated upon later in this report, the powerful combination of nanoscience and oxide interface engineering may potentially lead to development of new interface-property-driven electrode structures.

2.4 Discussion of selected recent systems

There is considerable content in the literature that suggests the benefits described above indeed are associated with performance enhancements for oxide photoanodes in PEC cells. Table 1 provides a summary of selected recent systems from the literature that highlight these findings. The table also includes the charge transfer among oxide phases suggested in the study. This summary is by no means comprehensive and is meant solely as an introduction to the recent research efforts dedicated to the design of oxide heterostructures for this application.

2.5 Nanoscale architectures

Various heterostructure architectures possessing nanoscale feature dimensionality show promise to effectively utilize the benefits described above. The concept of extremely thin-absorbers,³⁰ as established for photovoltaic devices, has been successfully applied in designs for oxide heterostructure photoanodes. In short, by placing the absorbing phase in intimate contact with a nanostructured conductive substrate, this technique permits the use of materials with small carrier diffusion lengths but large optical absorption lengths. Glasscock³¹ fabricated and characterized core-shell nanorod ZnO- α -Fe₂O₃ heterostructures using a combination of aqueous chemical synthesis and vapor phase deposition. Their characterization revealed the presence of α -Fe₂O₃→ZnO electron transfer during irradiation, and showed some long wavelength conversion enhancements associated with the architecture. The analysis suggested a significant energy barrier for electron injection from α -Fe₂O₃ into ZnO, which is consistent with expectations considering ZnO's greater electron affinity. Sivula *et al.*³² utilized a two-step atmospheric pressure CVD process to produce WO₃- α -Fe₂O₃ heterostructures, which showed

PEC enhancements at weakly absorbing long wavelengths, which was directly attributed to the presence of the nanostructured WO_3 substrate. Oblique-angle physical vapor deposition, which enables fabrication of nanostructured films using ballistic species transport and self-shadowing effects, has recently been used to fabricate WO_3 - TiO_2 core-shell nanostructures.³³ Charge transfer between the phases was observed and was associated with overall efficiency enhancements. A related nanoscale architecture was previously achieved by coating TiO_2 nanotubes with WO_3 by electrochemical deposition.³⁴

WO_3 and BiVO_4 were combined in a recent work by Su *et al.*³⁵ to efficiently utilize both the complimentary optical absorption of these materials and charge separation ability associated with their junction. Because the valence band edge of BiVO_4 contains contributions from Bi *s* states, it is situated at higher energies than that of WO_3 , and therefore provides an efficient mechanism for the separation of photogenerated holes during photanode operation. Their results showed considerable enhancements are associated with the heterostructure configuration. Nanoparticle heterostructures comprised of α - Fe_2O_3 and CoAl_2O_4 nanoparticles have shown PEC performance enhancements over bare p-type CoAl_2O_4 .³⁶ It was speculated that the differing conductivity types of the nanoparticles, organized in three dimensions, facilitated charge separation under irradiation.

Table 1. Summary of selected recent oxide heterostructure systems discussed in this report.

Heterostructure	Description	Fabrication methods	Suggested charge transfer		Ref.
			Electron	Hole	
$\alpha\text{-Fe}_2\text{O}_3 - \text{CoAl}_2\text{O}_4$	Nanoparticle composite	Doctor blading	$\alpha\text{-Fe}_2\text{O}_3 \rightarrow \text{CoAlO}_4$	$\text{CoAlO}_4 \rightarrow \alpha\text{-Fe}_2\text{O}_3$	36
$\alpha\text{-Fe}_2\text{O}_3 - \text{TiO}_2$	Bilayer film	Thermal growth; CVD	$\text{TiO}_2 \rightarrow \alpha\text{-Fe}_2\text{O}_3$	$\alpha\text{-Fe}_2\text{O}_3 \rightarrow \text{TiO}_2$	41
$\alpha\text{-Fe}_2\text{O}_3 - \text{WO}_3$	Bilayer film	Sol-gel	$\text{WO}_3 \rightarrow \alpha\text{-Fe}_2\text{O}_3$	none	40
$\text{WO}_3 - \alpha\text{-Fe}_2\text{O}_3$	Nanostructured composite	APCVD	$\alpha\text{-Fe}_2\text{O}_3 \rightarrow \text{WO}_3$	none	32
$\text{WO}_3 - \text{BiVO}_4$	Core-shell nanostructure arrays	Solvothermal technique; spin coating	$\text{BiVO}_4 \rightarrow \text{WO}_3$	$\text{WO}_3 \rightarrow \text{BiVO}_4$	35
$\text{WO}_3 - \text{BiVO}_4$	Bilayer film	Spin coating; polymer-assisted direct deposition	$\text{BiVO}_4 \rightarrow \text{WO}_3$	$\text{WO}_3 \rightarrow \text{BiVO}_4$	37,38
$\text{Fe}_2\text{O}_3 - \text{SrTiO}_3$	Bilayer film	Spin coating	$\text{SrTiO}_3 \rightarrow \text{WO}_3$	$\text{WO}_3 \rightarrow \text{SrTiO}_3$	39
$\text{WO}_3 - \text{TiO}_2$	Core-shell nanostructure arrays	Oblique-angle deposition	$\text{TiO}_2 \rightarrow \text{WO}_3$	$\text{WO}_3 \rightarrow \text{TiO}_2$	33
$\text{WO}_3 - \text{TiO}_2$	Coated nanotube arrays	Electrochemical anodization and deposition	none	none	34
$\text{ZnO} - \alpha\text{-Fe}_2\text{O}_3$	Core-shell nanostructure arrays	Aqueous chemical synthesis; filtered arc deposition	$\alpha\text{-Fe}_2\text{O}_3 \rightarrow \text{ZnO}$	none	31

2.5.1 Bilayers

In systems not limited by charge transport, simple bilayer heterostructures provide an effective means to utilize the complimentary functionalities of metal oxides. WO_3 and BiVO_4 bilayers have been studied comprehensively,^{37,38} and in general these configurations permit the simultaneous utilization of the transport properties of WO_3 as well as the optical absorption properties of BiVO_4 .³⁷ Similarly, Fe_2O_3 has been combined with the transparent wide-bandgap insulator SrTiO_3 ³⁹ for the purpose of charge separation, with consistent enhancements evident. $\text{WO}_3\text{-}\alpha\text{-Fe}_2\text{O}_3$ bilayer films show enhancements associated with formation of their junction.⁴⁰ Interestingly, an electrode comprised of a 120 nm TiO_2 surface layer on thermally grown $\alpha\text{-Fe}_2\text{O}_3$ was shown to exhibit energetic contributions from both phases.⁴¹ In general, the simple geometries of bilayer heterostructures provide systems that are suitable for fundamental analyses of prospective photoanode materials and especially of the potential benefits of junction formation.

2.5.2 Ultrathin coatings

In a discussion of oxide heterostructures with nanoscale dimensionality it is worthwhile to comment on the influence of ultra-thin surface coatings, and especially on their influence on $\alpha\text{-Fe}_2\text{O}_3$ -based photonodes. The poor water oxidation kinetics of $\alpha\text{-Fe}_2\text{O}_3$ focuses attention on the modification of surface states, toward increasing rate constants associated with electron transfer from hydroxyl ions in solution. It was shown that the deposition of tungsten oxide species on the surface of $\alpha\text{-Fe}_2\text{O}_3$ films increases the faradic rate constant for water oxidation.⁴² More recently

the α -Fe₂O₃ surfaces were passivated with ultrathin Al₂O₃⁴³ and Ga₂O₃⁴⁴ layers, which show consistent and positive effects on photoelectrochemical performance, including a cathodic shift of the photocurrent onset of α -Fe₂O₃. In general it can be expected that ultrathin coatings passivate surface states and therefore reduce the probability of electron-hole recombination associated with their presence. This is especially true for those oxides that are isostructural to α -Fe₂O₃.⁴⁴

2.6 The α -Fe₂O₃-WO₃ system

2.6.1 Introduction to material system

The above discussion above describes the motivation and framework for developing effective oxide heterostructures with nanoscale dimensionality for efficient solar water oxidation. The present section introduces and discusses in this provided context recent experimental work from the authors' laboratories.

Tungsten(VI) oxide (tungsten trioxide, WO₃) and its slightly reduced form WO_{3-x} are intensely studied as solar energy materials for their significant photoactivity under UV and blue light irradiation. In PEC devices, nanostructured WO₃ films produce high photocurrents for water oxidation, and are compatible with a number of tandem designs based on multiple photosystems.^{45,46} The material's ability to produce high, stable photocurrents for *sea water* splitting is considered an important discovery toward sustainable and economical solar fuel production.⁴⁷

Alpha-phase iron(III) oxide (hematite, α -Fe₂O₃) is highly abundant in Earth's crust and is widely utilized by a number of established and global industries. Nanostructured α -Fe₂O₃ in particular has proven to be a highly functional metal oxide for a number of energy applications. It has received considerable attention as a solar energy conversion material because its bandgap is well-suited for solar photon absorption and its high ionization potential yields a valence band appropriately positioned to accept charges toward the oxidation of water. The extreme low cost and chemical stability of α -Fe₂O₃ make its implementation into solar energy conversion devices highly attractive for the development of economical solar electricity and fuel production.

Figure 5 provides an illustration depicting the hetero-nanostructure design. Depending on the fabrication conditions and application at hand, these anisotropic composites might be described as nanoparticle-sensitized, core-shell, or radial-junction structures. In the present case, both materials are photoactive under solar irradiation when applied as electrodes in a PEC cell, as indicated in the illustration and described later in this report. The arrays were fabricated through application of a combination of aqueous chemical growth⁴⁸ and physical vapor deposition techniques (see Methods for details).

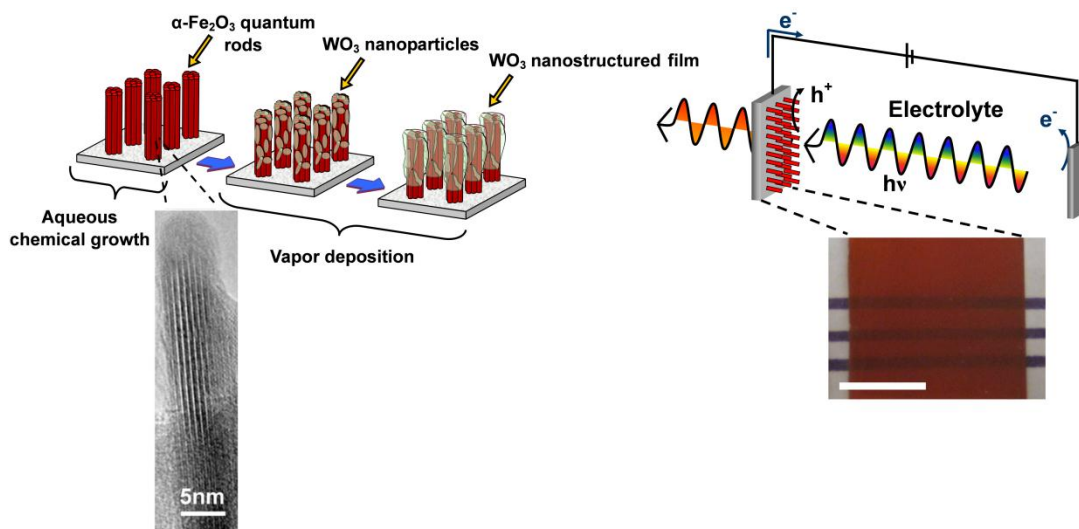


Figure 5. Illustration depicting the design of metal oxide hetero-nanostructure arrays and their application as photoanodes for photoelectrochemical cells. The HRTEM image shows an individual single-crystalline α - Fe_2O_3 quantum rod. The picture on the right shows the as-prepared sample (Scale bar indicates 1 cm)

2.6.2 Physical and optical characterization

The morphology of the arrays is examined through scanning electron microscopy and is presented in Figures 6a-e. Figure 6a shows the α - Fe_2O_3 nanorods produced by the hydrolysis-condensation and dehydration process.⁴⁸ The width of these rod bundles is approximately 50 nm and their length is approximately 800 nm. As indicated in the HRTEM image in Figure 2, they consist of 3-5 nm-diameter single crystals whose electrons are quantum-confined in the lateral dimension, which manifests as a cathodic shift (vs SHE) of the conduction band and a bandgap blue-shift.⁴⁹ They provide a very efficient pathway for both majority carriers (direct pathway along the vertically oriented rods) and minority carriers (hole diffusion length match with the quantum rod lateral dimensions).⁴⁹ The structures after modification with WO_3 are displayed in Figure 6b-d. The large internal surface area is maintained and the diameter of the structures increases with increasing deposition time indicating that the rods are coated with a thin layer of WO_3 during exposure to the deposition source. Similar coatings resulting from nanorod exposure to laser ablation plasmas have previously been observed for a ZnO-ZnSe system.⁵⁰ Figure 6e shows a cross sectional view of the structures after extended exposure. There is a slight gradient in thickness along the length of the rod, which is attributed to shadowing effects commonly encountered in vacuum deposition techniques.

The optical and structural properties of the hetero-nanostructures deposited onto 2.3 mm thick transparent conductive fluorinated tin oxide-coated soda lime glass ($\text{SnO}_2:\text{F}/\text{glass}$) are displayed in Figures 6f and 6g. All samples are deep red and transparent to lower-energy visible light (see representative sample photograph in Figure 2). The UV-vis-near IR spectrum of the hetero-nanostructures is presented in Figure 6h. The main absorption transition around 600 nm matches closely to those of the α - Fe_2O_3 nanorods,⁵¹ which is consistent with expectations considering the

larger bandgap of WO_3 . x-ray diffractograms (Figure 6h) indicate the presence of three distinct crystal phases: orthorhombic WO_3 , trigonal Fe_2O_3 (hematite), and the tetragonal SnO_2 (cassiterite) substrate.

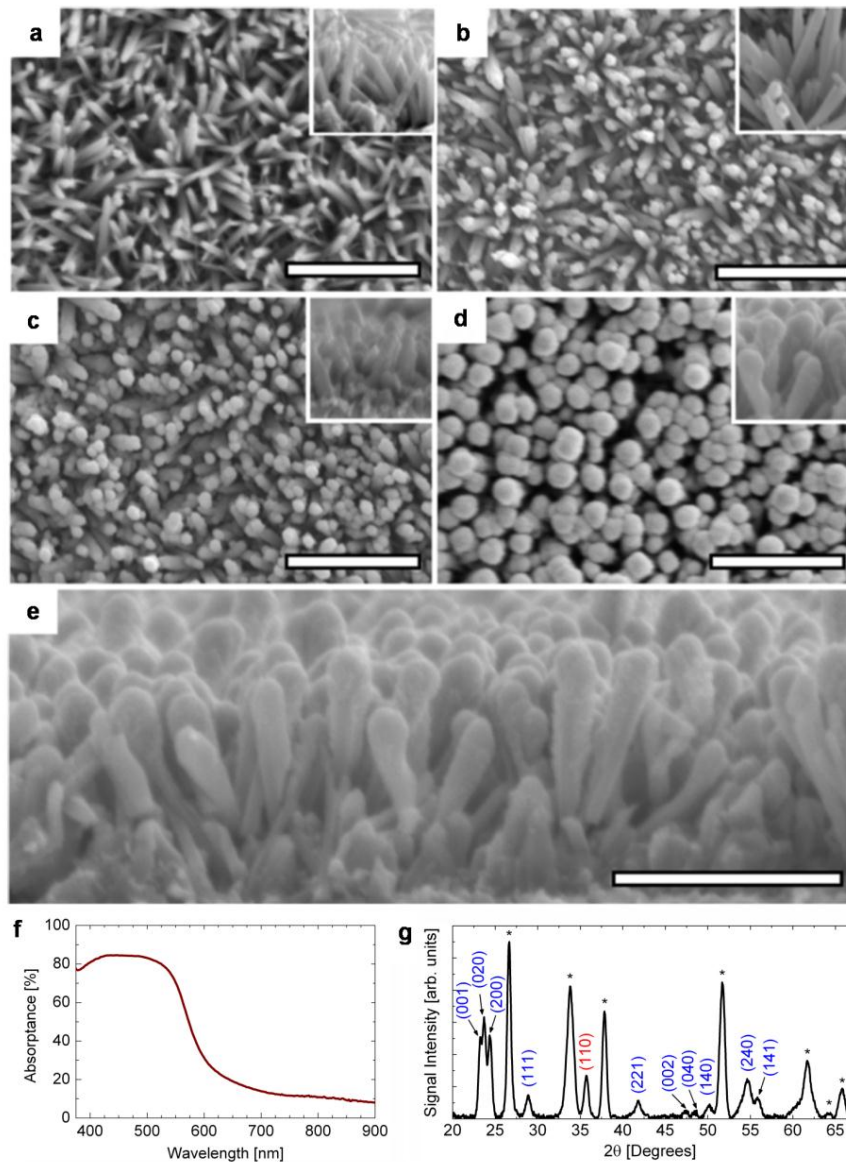


Figure 6. (a) SEM images of $\alpha\text{-Fe}_2\text{O}_3$ arrays as fabricated by aqueous chemical growth. (b)-(d) SEM images of arrays modified by WO_3 for increasing deposition times, indicating the evolution of the structure morphology. (e) SEM Cross-sectional view of hetero-nanostructure array after longest deposition time. All scale bars indicate 1 μm . Insets provide cross-sectional views at identical magnification. (f) UV-vis-near IR optical absorbance of $\alpha\text{-Fe}_2\text{O}_3\text{-WO}_3$. (g) x-ray diffraction pattern of the hetero-nanostructure array indicating the presence of orthorhombic WO_3 (blue), trigonal Fe_2O_3 (red), and tetragonal SnO_2 substrate (*).

2.6.3 Photoelectrochemistry

The samples have been applied as photoelectrodes in PEC cells for solar hydrogen generation. For this application, the interest in this system lies in the complimentary functionality offered by the two components. When the electrode is applied as an anode in a PEC cell for water photoelectrolysis, photogenerated holes participate in the water oxidation reaction and electrons travel to the back contact and enter the external circuit. The faradic rate constant for electron transfer from hydroxyl ions at the WO_3 surface is orders of magnitude greater than at the $\alpha\text{-Fe}_2\text{O}_3$ surface ($r_{\text{WO}_3} = 10^3\text{-}10^4 \text{ cm s}^{-1}$; $r_{\alpha\text{-Fe}_2\text{O}_3} = 0.1\text{-}1 \text{ cm s}^{-1}$),⁵² due to the superior kinetics of charge injection into O $2p$ bands. The modification of $\alpha\text{-Fe}_2\text{O}_3$ film surfaces with tungsten oxide species has been shown previously to increase the faradic rate constant for water oxidation.⁴² The hole diffusion length in WO_3 has been estimated to be about 150 nm,⁵³ two orders of magnitude higher than that estimated for $\alpha\text{-Fe}_2\text{O}_3$, 2-4 nm⁵⁴. Despite these advantages, the theoretical maximum water splitting efficiency of WO_3 remains low due to insufficient overlap between its optical absorption and the solar spectrum. The bandgap of $\alpha\text{-Fe}_2\text{O}_3$ on the other hand is nearly ideal, which results in a theoretical efficiency of 12.9 %.⁵⁵ The ultrafine $\alpha\text{-Fe}_2\text{O}_3$ nanorods utilized in this study were first designed and fabricated by Vayssieres *et al.* with the small hole diffusion length of $\alpha\text{-Fe}_2\text{O}_3$ in mind; their photoelectrochemistry has been documented.^{51,56}

The hetero-nanostructure arrays and the bare $\alpha\text{-Fe}_2\text{O}_3$ electrodes were studied in a two-electrode configuration for solar hydrogen generation. Figure 7a shows chopped-light current-potential behavior in an aqueous 0.5 M NaCl solution with solar-simulated 100 mW cm^{-2} AM 1.5G-filtered (1 sun) irradiation; Figure 7b provides an incident photon conversion efficiency (IPCE) spectrum. The sodium chloride solution is chosen for its similarity to the composition of filtered sea water; under these conditions the thermodynamically favorable electrochemical reactions are the hydrogen, oxygen (and potentially chlorine at high bias) gas evolution reactions. No sacrificial reagents are employed and the solution is neutral. All PEC results presented indicate that the arrays behave as photoanodes in these electrolytic conditions; that is, a positive photocurrent is observed at applied anodic potential.

These PEC data suggest that a significant quantity of holes originating from visible-light excitations is extracted before recombining with electrons traveling to the back contact. This is confirmed in the IPCE spectrum, which shows spectral response beyond 550 nm. Considering the transparency of WO_3 to visible light ($E_{\text{gap}} \sim 3 \text{ eV}$), these low energy excitations must occur either in the $\alpha\text{-Fe}_2\text{O}_3$ core, or at intra-bandgap defect, surface, or interface states in WO_3 . The electrode operation is discussed below in the context of its physical design and its potential for possessing anomalous electronic characteristics.

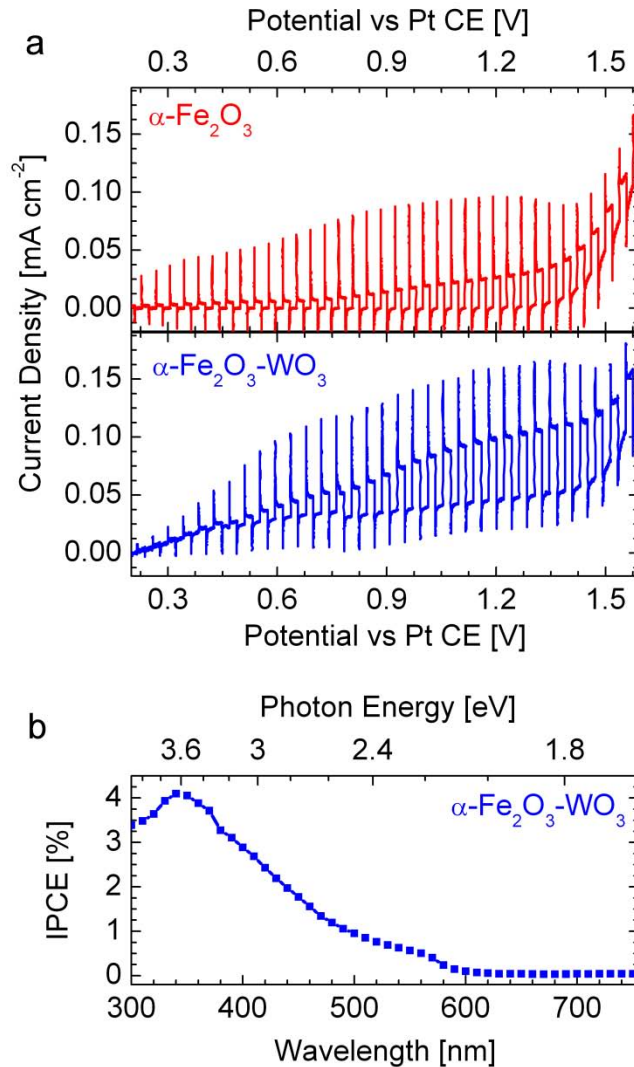


Figure 7. Photoelectrochemical characterization in aqueous 0.5 M NaCl solution: (a) Photocurrent-potential curve under chopped (0.2 s^{-1}), 100 mW cm^{-2} AM 1.5G-filtered solar-simulated irradiation. Potential applied vs a Pt CE. (b) IPCE spectrum with +1 V applied versus a Pt counter electrode. Data correspond to arrays fabricated as those in Figure 6c.

The hetero-nanostructure architecture demands electron transport through the $\alpha\text{-Fe}_2\text{O}_3$ rods in order for the PEC cell to register photocurrent in the external circuit. Conduction band electron transport between the layers is therefore a topic of interest. Results in previous reports of $\alpha\text{-Fe}_2\text{O}_3\text{-WO}_3$ composite photoanodes suggest electron transfer occurs in either direction under applied anodic potential.^{32,40} Understanding of the band alignment in the present system is complicated by the quantum confinement effect in the $\alpha\text{-Fe}_2\text{O}_3$ rods (Reference 49 indicates the electron affinity is near 0 V vs SHE).

Simultaneously, the oxidation reaction must occur in order to limit the recombination of free carriers, and therefore holes must be present at the hetero-nanostructure-liquid interface to accept

charges from electrolyte species. From the viewpoint of bulk semiconductor physics, it is expected that there is an energy barrier of ca. 0.5 eV⁵⁷ for hole injection from α -Fe₂O₃ into WO₃, due to the energetic difference between O 2*p* orbitals, of which the valence band of WO₃ is comprised, and the Fe *d* levels at which holes arrive at the α -Fe₂O₃ surface (it is likely that holes arrive at the surface in a band of e_g levels, which are expected to be the highest occupied orbitals in α -Fe₂O₃⁵²). The observation of photoactivity originating from visible light excitations could involve phenomena directly related to the nanoscale architecture. Indeed, at the length scales considered here, the interfacial region is expected to play an important role in the electronic band construction. In transition metal oxide heterostructures, interface electronic orbital reconstruction has been reported by a number of mechanisms, depending on the precise nature of the chemical bonds at the interface.⁵⁸ Considering the very high density of interface states in this system, owing to the nanoscale particle dimensions, it is feasible the valence band consists of hybridized orbitals with character resulting from both metal oxides and their surface configurations. The electronic character of the α -Fe₂O₃-WO₃ interface is expected to be extremely complex, and depend on several interface system properties, including charge transfer and orbital hybridization. Understanding these interface properties requires intense experimental investigations, the strategies for which are being studied in the authors' laboratories.⁵⁹

Alternatively, due to the physical dimensions of the α -Fe₂O₃ structures (ca. 5 nm lateral dimension⁴⁹) and thin WO₃ layers, quantum-mechanical tunneling processes must be considered for hole extraction from the core. The transfer of holes from α -Fe₂O₃ to an electrolyte through TiO₂, which also has a valence band edge derived from O 2*p* orbitals, was reported as early as 1982⁴¹ and was attributed to a tunneling process. Reference 41 also suggests that band banding at the semiconductor-liquid interface could potentially extend through both phases in heterostructure photoelectrodes. If this is the case during operation of the present electrodes, depletion effects and upward band banding could assist in overcoming energy barriers for charge transfer from α -Fe₂O₃ to the electrolyte. It is unknown to what extent band banding exists in the α -Fe₂O₃-WO₃ electrodes; numerous previous studies suggest these effects are absent in nanostructured electrodes in contact with electrolytes.^{60,61,62} Exciting work is currently being conducted in this area: a recent study from Augustynski and coworkers⁶³ suggests that during operation proton intercalation induces a structural change in mesoporous WO₃ electrodes, which results in a core-shell structure.

In the PEC configurations studied above, the electrode photocurrent response is remarkably similar to those found in previous studies of α -Fe₂O₃ nanorod arrays.^{51,56,64} In addition, the photoelectrochemical characterization instrumentation employed was not precise enough to identify differences among samples with varying WO₃ thickness. Indeed, these PEC performance similarities most likely result from the current-limiting effect of the undoped α -Fe₂O₃ core, which is expected to be highly resistive.⁶⁵ These observations suggest that more in-depth optoelectronic characterization techniques are required to elucidate the complex charge transfer processes present in quantum-confined metal oxide hetero-nanostructures containing *d*-shell electrons. To this end the hetero-nanostructures' carrier dynamics were examined by ultrafast transient absorption spectroscopy.

2.6.4 Ultrafast transient absorption spectroscopy

The ultrafast carrier dynamics of α -Fe₂O₃ thin films, single crystals, and nanoparticle suspensions have been comprehensively examined.^{66,67,68,69} It is observed that intraband carrier thermalization occurs on extremely fast times scales (< 150 fs;⁶⁶ < 75 fs⁶⁸). Transient absorption signals at longer times are therefore attributed to relaxation of excited electrons to a dense manifold of electronic states within the bandgap and valence band, resulting from both intrinsic defects and surface states.⁶⁶ However, the assignment of transient absorption signals to specific physical correlates in this complex material system must be conducted in the context of all available information. This includes the many studies performed over the past few decades,^{66,67,68,69,70} including several recent advances,^{71,72} with numerous signal assignments proposed. In general the analysis is complicated by the *d-d* transitions present over spectral ranges commonly probed. Analyses of carrier dynamics of α -Fe₂O₃ nanomaterials is complicated in addition by high densities of surface states, which may introduce new decay pathways.

Of particular relevance to the present analysis is a recent report from Durrant and colleagues,⁷² which describes the use of a hole-scavenging sacrificial chemical to determine the correspondence of the transient absorption signal at 580 nm to unoccupied valence band states (holes) in α -Fe₂O₃. The following discussion is presented in the context of this and other studies of excited carrier dynamics in related material systems.

The samples were pumped with 540 nm (2.29 eV) 130 fs pulses, which excite the α -Fe₂O₃ core near the weak Fe $3d \rightarrow 3d$ transition.⁵ The transient absorbance spectrum of a representative α -Fe₂O₃-WO₃ sample is presented in Figure 8a at 500 fs after excitation. Absorption difference signals at various probe energies reflect the populations of electronic states with corresponding absorption energies after excitation. A broad distribution of absorbance signals over the studied wavelength range is evident at this delay time. Spectra of this type have been previously observed in femtosecond relaxation studies of iron oxide particulate suspensions.⁶⁸ These studies concluded that because the electron relaxation processes possess both a fast (~ 1 ps) and slower (~ 10 ps) decay over the entire probe spectrum, they may correspond to a common physical process – for instance, the capture of electrons by oxygen-deficient centers of Fe³⁺.⁶⁸ As observed below, all relaxation processes exhibit both a sub-picosecond fast component as well as a longer component extending to hundreds of picoseconds.

Figures 8b-e show the normalized transient absorption signals for α -Fe₂O₃ and α -Fe₂O₃-WO₃ at two probe wavelengths, 579.31 nm (2.14 eV) and 674.23 nm (1.84 eV), in two time regimes. For both energies, there is an ultrafast rise in signal intensity limited by the laser pulse. Examination of the transient absorption at the picosecond time scale (Figures 8b,c) reveals the fast components of the kinetics for both probe energies are very similar before and after modification with WO₃. Because the time signatures of the signals' rise and decay overlap at this scale, the corresponding fast physical processes apparently occur irrespective of the presence of surface modification.

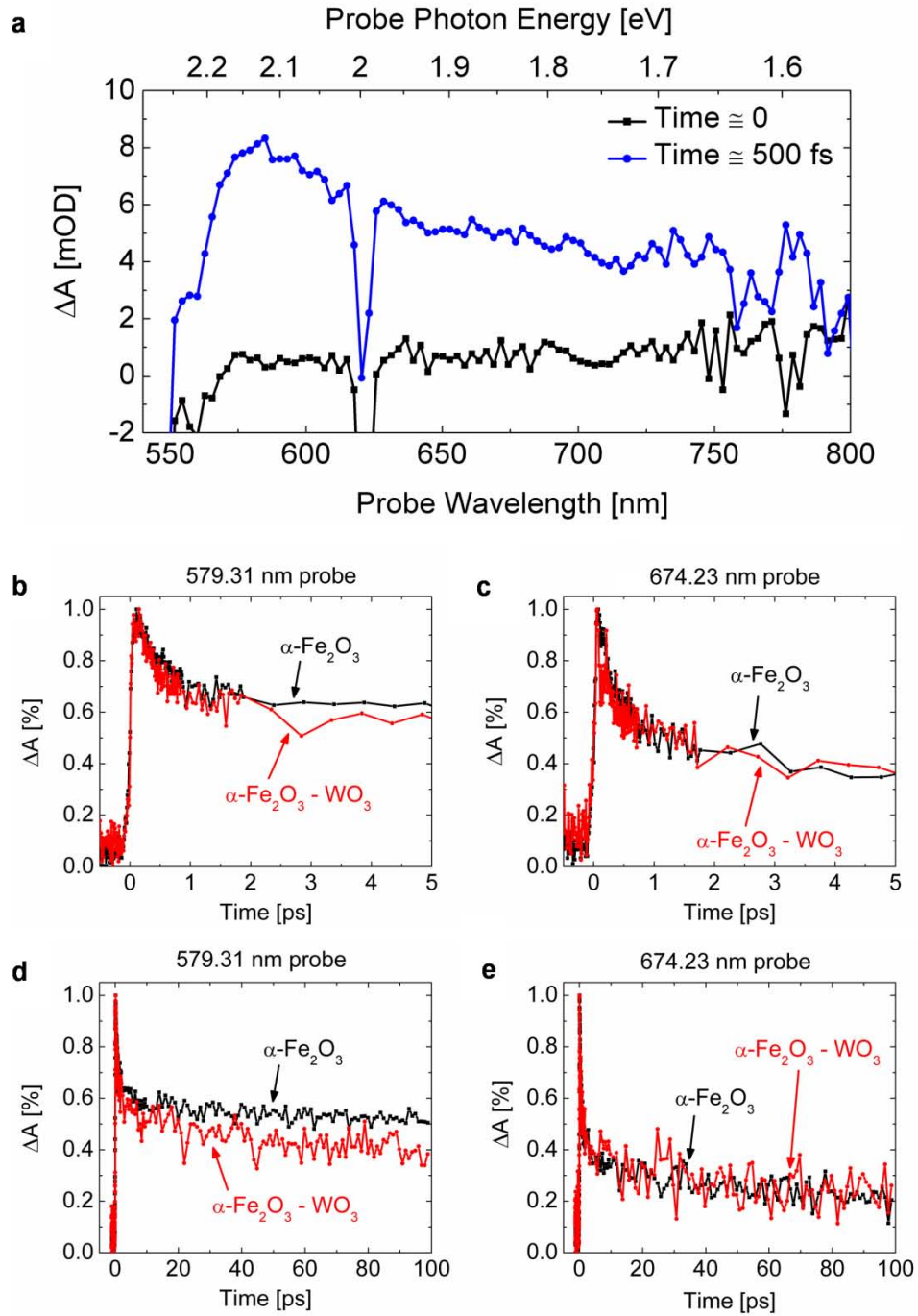


Figure 8. Ultrafast transient absorption spectroscopy for hetero-nanostructure electrodes: (a) Transient difference absorbance spectra for $\alpha\text{-Fe}_2\text{O}_3\text{-WO}_3$ before excitation (black squares) and 500 fs after excitation (blue circles). Transient absorption signals for $\alpha\text{-Fe}_2\text{O}_3$ (black) and $\alpha\text{-Fe}_2\text{O}_3\text{-WO}_3$ (red) at the picosecond time scale for 579.31 nm probe (b) and 674.23 nm probe (c) and the sub-nanosecond time scale for 579.31 nm probe (d) and 674.23 nm probe (e).

Additional information is provided by the transient absorption at longer time scales (Figures 8d,e). For all probe wavelengths examined, following the initial fast process, there is a slow process that persists to beyond 100 ps. The most notable feature of these data is that the normalized transient absorption signal at 579.31 nm decays at a faster rate for α -Fe₂O₃-WO₃ than for α -Fe₂O₃. Considering that the transient absorption signal signifies the occupation of an electronic state at a given delay time, a faster destruction of the absorption signal at 579.31 nm may suggest a faster destruction (removal) of unoccupied states (holes) from the probed system. It is observed that the accelerated decay is nonexistent for the lower energy transition recorded at 674.23 nm. Alternatively, it is possible the decays represent a trapping process, and the introduction of the WO₃ phase enhances the trapping rate of electrons within a particular range of corresponding probe energies. Trapped electrons in this case possess a low extinction coefficient, which manifests as an attenuation of the associated probe signal.

Given the knowledge that α -Fe₂O₃ nanomaterials possess many midgap states, associated with both the *d* levels and high surface areas, the wavelength dependence could describe migration of photoexcited electrons from conduction bands into shallow levels and deep traps. In this case, the associated recombinations evolve over the spectral range probed.

Upon examination of the decay kinetics over the complete probe spectrum, it is found that the signals' attenuation difference upon creation of a α -Fe₂O₃-WO₃ interface is determined by the energetic position of the corresponding electronic state. Larger probe energies, near the bandgap of α -Fe₂O₃, exhibit the largest signal difference upon creation of an α -Fe₂O₃-WO₃ interface. Indeed, the aforementioned study on operating α -Fe₂O₃-based PEC cells⁷² indicates that the removal of surface-trapped holes from α -Fe₂O₃ corresponds to decay in 580 nm absorption after excitation. Adoption of this assignment in the present study suggests that modification of α -Fe₂O₃ nanostructures with WO₃ promotes the extraction of surface-trapped holes on picosecond time scales.

These observations, when connected to the PEC results and band structure descriptions provided above, indicate the possible existence of anomalous carrier transport dynamics upon photoexcitation of the hetero-nanostructures.

2.7 Electronic structure of heterostructure interfaces

A number of the device performance enhancements associated with the use of nanomaterials relate directly to high surface areas and high densities of surface electronic states. Oxide hetero-nanostructures possess high *interfacial* areas, which can similarly be expected to contribute significantly to their electronic structures and therefore performance of electronic devices into which they are integrated.

The mechanisms by which oxide heterostructure interfaces are found to possess emergent functionality has been recently discussed⁷³ in a summary of the variety of physical phenomena associated with their fabrication. The summary proposes several strategies to tune the interface system's degrees of freedom, including charge transfer, epitaxial strain, symmetry breaking, electrostatic coupling, and frustration.⁷³ In addition to those effects isolated at interfaces, it is noted that several phenomena extend well away from interfaces. These phenomena include

unscreened Coulomb interactions as well as relaxations toward bulk properties away from the interface, which result in gradients of structure, polarization, and magnetization properties.

In the oxides of the transition metals, the *d* orbital character and occupancy critically influences the interaction of metal ions, and by extension the physical properties of these materials. Recent experiments conducted in the authors' laboratories⁵⁹ indicate that the formation of heterostructures comprised of titanium oxide and iron oxide nanomaterials, both of which are intensely investigated for photoelectrochemical applications, results in a number of modifications to the orbital character of the interface. Most importantly, it was found that the *d* orbitals in the interfacial region were enriched with electrons, which has a number of implications for devices utilizing transitions to and from their associated electronic states. In addition, through examination of the oxygen site environment, these studies provided evidence that the interface possessed an emergent degree of *p-d* orbital hybridization that was directly associated with formation of the heterojunction. These results provide confirmation of applicability of the principles of transition metal oxide interface engineering to the design of oxide heterostructure photoelectrodes for solar water splitting cells.

2.8 Conclusions

A perspective on the design of oxide heterostructure photoanodes for solar water oxidation has been presented. Performance enhancements can be associated with increased optical absorption, efficient charge separation across heterojunctions, kinetic advantages, and potentially with the engineering of interface electronic characteristics.

The demonstration of the successful combination of large-scale chemical and vapor phase synthesis techniques for the fabrication of vertically oriented metal oxide hetero-nanostructures without template, surfactant or applied fields toward solar energy conversion is of direct relevance to optimized (doped) nanostructured oxide materials. These results suggest that through this novel nanoscale architecture it is possible to engineer interesting or unexpected interfacial minority carrier transport properties for PEC applications of metal oxide hetero-nanostructures. The constituent oxides are highly functional nanomaterials for a number of applications and as such the hetero-nanostructure array is expected to display further functionalities, as well as to pave the way to cost-effective, large scale, hetero-nanostructure devices for solar energy conversion.

2.9 Methods

The fabrication procedure of arrays in this work consists of application of a combination of solution chemistry and physical vapor deposition techniques. The α -Fe₂O₃ nanorod arrays were first fabricated onto SnO₂:F-coated glass (FTO; Pilkington TEC7) following the procedure for hydrolysis-condensation described in detail in reference 48. For PEC characterization, the samples were annealed in air 700 °C. The WO₃ layer was fabricated by deposition of species from pulsed laser ablation of a rotating (10 rpm) pressed polycrystalline WO₃ target in O₂ ambient (reactive pulsed laser deposition) using a Lambda Physik LPX 200 KrF Excimer Laser (248 nm). A stainless steel chamber was evacuated to a base pressure about 10⁻⁴ torr, after which O₂ gas (industrial grade) was flowed through the evacuated chamber for 30 minutes at 18 sccm,

as set by a mass flow controller, to replace residual gases. The α -Fe₂O₃/FTO sample was mounted on a substrate holder using conductive Ag paste. Deposition occurred at a laser fluence of $\sim 1 \text{ J cm}^{-2}$ per pulse with pulse frequency of 9 Hz for various times. Figures 6b-6e show samples from deposition times of 5, 10, 16, and 16 minutes, respectively. The O₂ pressure during deposition was approximately 4×10^{-3} torr as measured by a pirani pressure gauge. Before deposition the target was ablated for a several minutes at the deposition laser parameters to remove any contaminants from the target surface, during which the entire substrate was masked with a mechanical shutter. Throughout deposition the sample was maintained at 100 °C using a resistance heater and thermocouple embedded in the substrate holder. After deposition the chamber was sealed and the sample was allowed to cool to room temperature in the quiescent low-pressure O₂ ambient. After the sample was removed it was annealed in air at 400 °C for 2 hours (the ramp rate to 400 °C was approximately 1.5 °C /min).

2.9.1 Physical characterization

Scanning electron microscopy (SEM) images were obtained with a Hitachi environmental field emission scanning electron microscope (Model S-4300SE/N) with an accelerating voltage of 3-5 kV, operating in secondary electron detection mode.

Spectral transmittance and reflectance measurements were taken on the α -Fe₂O₃-WO₃/SnO₂:F/glass samples with a Perkin Elmer Lambda Spectrophotometer fitted with an integrating sphere over the wavelength range 375 nm to 900 nm at a wavelength interval of 2 nm. The sample was irradiated from the α -Fe₂O₃-WO₃ surface. The spectral absorbance was obtained by solution of the equation $A_\lambda = (100 - R_\lambda - T_\lambda) - A_{\lambda, \text{FTO}}$.

X-ray diffraction data were obtained with Cu K α radiation from a commercial diffractometer.

2.9.2 Photoelectrochemical characterization

The electrolyte was prepared with 18.1 M Ω -cm water with 0.5 M NaCl (Sigma Aldrich; 98%). An electrical contact was made to the SnO₂:F electrode with a conductive silver paste and copper wire. Photoelectrochemical measurements were made in an open pyrex cell fitted with 3 mm thick quartz window. A 1 cm² masked-off, sealed area of the sample was irradiated with a 300 W Xe bulb solar simulator with adjustable power settings through an AM 1.5G filter (Oriel; 81092). The light intensity at the sample location in the photoelectrochemical cell was 100 mW cm⁻² as measured by a power detector (Newport; 70284). No correction was made for the optical absorption of the 4 cm of electrolyte between the quartz window and sample location. A potentiostat (Pine Instruments Bipotentiostat) was used to measure electrochemical data in a two-electrode setup using a coiled Pt wire counter electrode. N₂ gas was continuously bubbled in solution and directly over the Pt counter electrode before and during the experiment to remove any dissolved O₂ and therefore suppress the reduction of dissolved O₂ at the counter electrode. For current-potential measurements, the potential scan was anodic (in the positive direction) and at a rate of 5 mV s⁻¹, with the light mechanically chopped every ten seconds. To measure IPCE spectrum, a monochromator was used to select wavelengths (10 nm interval) from the chopped (5 Hz) output of a 70 W Xe bulb solar simulator. The incident photon flux at each wavelength

was measured by diverting a portion of the beam with a beam splitter into a calibrated silicon photodiode.

2.9.3 Ultrafast transient absorption spectroscopy

The ultrafast laser system is based on a Quantronix femtosecond laser system,⁷⁴ consisting of an Er-doped fiber oscillator, a regenerative/multi-pass amplifier, and a diode-pumped, Q-switched, second harmonic Nd:YLF pump laser (527 nm, 10 W capacity). Before injection into the amplifier, chirped pulse amplification is performed to temporally stretch, amplify, and recompress the initial short pulse, resulting in a pulse near its original duration, albeit with a vastly higher energy level (sub-nJ raised to mJ). After amplification, the as-generated fundamental (795 nm) is beam-split to generate both a white light continuum (WLC) probe pulse as well as feeding a tunable optical parametric amplifier (OPA) consisting of two delay stages: a signal pre-amplification stage and a power amplification stage. The output of the OPA was passed through wavelength separators in order to achieve a tunable pump wavelength. The system operates at 750 Hz repetition rate.

The final output was ca. 130 fs pulses centered at 540 nm excitation wavelength which was attenuated with neutral density filters. The pump beam was overlapped spatially and temporally with the WLC probe beam at the sample. The time delay between the pump and probe beams was controlled by a translation stage with 1 μm resolution. Each sample was tested for four cycles to achieve a lower-noise average response.

2.10 References

1. A. Brinkman, M. Huijben, M. van Zalk, J. Huijben, U. Zeitler, J. C. Maan, W. G. van der Wiel, G. Rijnders, D. H. A. Blank and H. Hilgenkamp, *Nature Mat.*, 2007, **6**, 493-496.
2. A. Ohtomo and H.Y. Hwang, *Nature*, 2004, **427**, 423-426.
3. J. Garcia-Barriocanal, A. Rivera-Calzada, M. Varela, Z. Sefrioui, E. Iborra, C. Leon, S. J. Pennycook and J. Santamaria, *Science*, 2008, **321**, 676-680.
4. L. Duan, L. Tong, Y. Xu and L. Sun, *Energy Environ. Sci.*, 2011, Advance Article, DOI: 10.1039/C1EE01276B.
5. *On Solar Hydrogen & Nanotechnology*, Ed: L. Vayssieres, John Wiley & Sons, Singapore, 2009.
6. X. Chen, S. Shen, L. Guo and S. S. Mao, *Chem. Rev.*, 2010, **110**, 6503-6570.
7. M. G. Walter, E. L. Warren, J. R. McKone, S. W. Boettcher, Q. Mi, E. A. Santori and N. S. Lewis, *Chem. Rev.*, 2010, **110**, 6446-6473.

8. Y. Lin, G. Yuan, S. Sheehan, S. Zhou and D. Wang, *Energy Environ. Sci.*, 2011, Advance Article DOI: 10.1039/C1EE01850G.
9. K. Sivula, F. Le Formal and M. Grätzel, *ChemSusChem*, 2011, **4**, 432-444.
10. J. Sun, D. K. Zhong and D. R. Gamelin, *Energy Environ. Sci.*, 2010, **3**, 1252-1261.
11. Y. Lin, G. Yuan, R. Liu, S. Zhou, S. W. Sheehan and D. Wang, *Chem. Phys. Lett.*, 2011, **507**, 209-215.
12. A. J. Nozik, *Nano Lett.*, 2010, **10**, 2735-2741.
13. H. A. Atwater and A. Polman, *Nature Mat.*, 2010, **9**, 205-213.
14. P. V. Kamat, *J. Phys. Chem. C*, 2007, **111**, 2834-2860.
15. *Nanostructured and Photoelectrochemical Systems for Solar Photon Conversion*, Eds: M. D. Archer, A. J. Nozik, Imperial College Press, London, 2008.
16. X. Chen and S. S. Mao, *Chem. Rev.*, 2007, **107**, 2891-2959.
17. H. G. Park and J. K. Holt, *Energy Environ. Sci.*, 2010, **3**, 1028-1036.
18. M. C. Putnam, S. W. Boettcher, M. D. Kelzenberg, D. B. Turner-Evans, J. M. Spurgeon, E. L. Warren, R. M. Briggs, N. S. Lewis and H. A. Atwater, *Energy Environ. Sci.*, 2010, **3**, 1037-1041.
19. M. D. Kelzenberg, S. W. Boettcher, J. A. Petykiewicz, D. B. Turner-Evans, M. C. Putnam, E. L. Warren, J. M. Spurgeon, R. M. Briggs, N. S. Lewis and H. A. Atwater, *Nature Mat.*, 2010, **9**, 239-244.
20. I. Thomann, B. A. Pinaud, Z. Chen, B. M. Clemens, T. F. Jaramillo and M. L. Brongersma, *Nano Lett.*, 2011, **11**, 3440-3446.
21. L. Vayssieres, A. Hagfeldt and S. -E. Lindquist, *Pure Appl. Chem.*, 2000, **72**, 47-52.
22. N. S. Lewis, *J. Electroanal. Chem.*, 2001, **508**, 1-10.
23. M. Grätzel, *Inorg. Chem.*, 2005, **44**, 6841-6851.
24. X. Chen, L. Liu, P. Y. Yu and S. S. Mao, *Science*, 2011, **331**, 746-750.
25. H. Zhong, Y. Zhou, Y. Yang, C. Yang and Y. Li, *J. Phys. Chem. C*, 2007, **111**, 6538-6543.

26. H. J. Snaith and C. Ducati, *Nano Lett.*, 2010, **10**, 1259-1265.
27. N. O. V. Plank, I. Howard, A. Rao, M. W. B. Wilson, C. Ducati, R. S. Mane, J. S. Bendall, R. R. M. Louca, N. C. Greenham, H. Miura, R. H. Friend, H. J. Snaith and M. E. Welland, *J. Phys. Chem. C*, 2009, **113**, 18515-18522.
28. H. H. Kung, H. S. Jarrett, A.W. Sleight and A. Ferretti, *J. Appl. Phys.*, 1977, **48**, 2463-2469.
29. A. Paracchino, V. Laporte, K. Sivula, M. Grätzel and E. Thimsen, *Nature Mat.*, 2011, **10**, 456-461.
30. K. Ernst, A. Belaidi and R. Könenkamp, *Semicond. Sci. Technol.*, 2003, **18**, 475-479.
31. J. A. Glasscock, PhD Thesis, University of New South Wales, Australia, 2008, 1-220.
32. K. Sivula, F. Le Formal and M. Grätzel, *Chem. Mater.*, 2009, **21**, 2862-2867.
33. W. Smith, A. Wolcott, R. C. Fitzmorris, J. Z. Zhang and Y. Zhao *J. Mater. Chem.*, 2011, **21**, 10792-10800.
34. J. H. Park, O. O. Park and S. Kim, *Appl. Phys. Lett.*, 2006, **89**, 163106.
35. J. Su, L. Guo, N. Bao and C. A. Grimes, *Nano Lett.*, 2011, **11**, 1928-1933.
36. K. -S. Ahn, Y. Yan, M. -S. Kang, J. -Y. Kim, S. Shet, H. Wang, J. Turner and M. Al-Jassim, *Appl. Phys. Lett.*, 2009, **95**, 022116.
37. S. J. Hong, S. Lee, J. S. Jang and J. S. Lee, *Energy Environ. Sci.*, 2011, **4**, 1781-1787.
38. P. Chatchai, Y. Murakami, S. -y. Kishioka, A. Y. Nosaka and Y. Nosaka, *Electrochim. Acta*, 2009, **54**, 1147-1152.
39. Y. Wang, T. Yu, X. Chen, H. Zhang, S. Ouyang, Z. Li, J. Ye and Z. Zou, *J. Phys. D: Appl. Phys.*, 2007, **40**, 3925-3930.
40. W. Luo, T. Yu, Y. Wang, Z. Li, J. Ye and Z. Zou, *J. Phys. D: Appl. Phys.*, 2007, **40**, 1091-1096.
41. F. -T. Liou, C. Y. Yang and S. N. Levine, *J. Electrochem. Soc.*, 1982, **129**, 342-345.
42. T. Kishi and M. Aritsuka, *Surf. Coat. Tech.*, 1998, **34**, 345-353.

43. F. Le Formal, N. Tétreault, M. Cornuz, T. Moehl, M. Grätzel and K. Sivula, *Chem. Sci.*, 2011, **2**, 737-743.
44. T. Hisatomi, F. Le Formal, M. Cornuz, J. Brillet, N. Tétreault, K. Sivula and M. Grätzel, *Energy Environ. Sci.*, 2011, **4**, 2512-2515.
45. J. Augustynski, G. Calzaferri, J. C. Courvoisier and M. Grätzel, in *Proc. of the 11th World Hydrogen Energy Conference*, Eds: T. N. Veziroglu, C. J. Winter, J. P. Baselt, G. Kreysa, Stuttgart, 1996, 2379.
46. E. L. Miller, R. E. Rocheleau and X. M. Deng, *Int. J. Hydrogen Energy*, 2003, **28**, 615-623.
47. J. Augustynski, R. Solarska, H. Hagemann and C. Santato in *Proc. SPIE*, **6340**, Ed. L. Vayssieres, *SPIE Press*, Bellingham, 2006, 63400J-1.
48. L. Vayssieres, N. Beermann, S.-E. Lindquist and A. Hagfeldt, *Chem. Mater.*, 2001, **13**, 233-235.
49. L. Vayssieres, C. Sathe, S. M. Butorin, D. K. Shuh, J. Nordgren and J. Guo, *Adv. Mater.*, 2005, **17**, 2320-2323.
50. K. Wang, J. Chen, W. Zhou, Y. Zhang, Y. Yan, J. Pern and A. Mascarenha, *Adv. Mater.*, 2008, **20**, 3248-3253.
51. N. Beermann, L. Vayssieres, S. -E. Lindquist and A. Hagfeldt, *J. Electrochem. Soc.*, 2000, **147**, 2456-2461.
52. M. P. Dare-Edwards, J. B. Goodenough, A. Hamnett and P. R. Trevellick, *J. Chem. Soc., Faraday Trans. 1*, 1983, **79**, 2027-2041.
53. M. A. Butler, *J. Appl. Phys.*, 1977, **48**, 1914-1920.
54. J. H. Kennedy and K. W. Frese, *J. Electrochem. Soc.*, 1978, **125**, 709-714.
55. A. B. Murphy, P. R. F. Barnes, L. K. Randeniya, I. C. Plumb, I. E. Grey, M. D. Horne and J. A. Glasscock, *Int. J. Hydrogen Energy*, 2006, **31**, 1999-2017.
56. T. Lindgren, H. Wang, N. Beermann, L. Vayssieres, A. Hagfeldt and S. -E. Lindquist, *Sol. Energy Mat. & Sol. Cells*, 2002, **71**, 231-243.
57. M. Grätzel, *Nature*, 2001, **414**, 338-344.

58. J. Chakhalian, W. Freeland, H. -U. Habermeier, G. Cristiani, G. Khaliullin, M. van Veenendaal and B. Keimer, *Science*, 2007, **318**, 1114-1117.
59. C. X. Kronawitter, J. R. Bakke, D. A. Wheeler, W. -C. Wang, C. Chang, B. R. Antoun, J. Z. Zhang, J. Guo, S. F. Bent, S. S. Mao and L. Vayssieres, *Nano Lett.*, 2011, **11**, 3855.
60. J. Nelson, *Phys. Rev. B*, 1999, **59**, 15374-15380.
61. F. Cao, G. Oskam, G. J. Meyer, and P. C. Searson, *J. Phys. Chem.*, 1996, **100**, 17021-17027.
62. I. Cesar., K. Sivula., A. Kay., R. Zboril and Michael Grätzel, *J. Phys. Chem. C*, 2009, **113**, 772-782.
63. A. Królikowska, P. Barczuk, R. Jurczakowski and J. Augustynski, *J. Electroanal. Chem.*, 2011, DOI: 10.1016/j.jelechem.2011.07.003
64. Y. Ling, G. Wang, D. A. Wheeler, J. Z. Zhang and Y. Li, *Nano Lett.*, 2011, **11**, 2119-2125.
65. F. J. Morin, *Phys. Rev.*, 1964, **93**, 1195-1199.
66. N. J. Cherepy, D. B. Liston, J.A. Lovejoy, H. Deng and J. Z. Zhang, *J. Phys. Chem. B*, 1998, **102**, 770-776.
67. A. G. Joly, J. R. Williams, S. A. Chambers, G. Xiong, W. P. Hess and D. M. Laman, *J. Appl. Phys.*, 2006, **99**, 053521.
68. V. A. Nadtochenko, N. N. Denisov, V. Y. Gak, F. E. Gostev, A. A. Titov, O. M. Sarkisov and V. V. Nikandrov, *Russ. Chem. Bull. Int. Ed.*, 2002, **51**, 457-461.
69. Y. P. He, Y. M. Miao, C. R. Li, S. Q. Wang, L. Cao, S. S. Xie, G. Z. Yang, B. S. Zou and C. Burda, *Phys. Rev. B*, 2005, **71**, 125411.
70. N. M. Dimitrijevic, D. Savic, O. I. Micic, and A. J. Nozik, *J. Phys. Chem.* 1984, **88**, 4278-4283.
71. A. J. Cowan, C.J. Barnett, S.R. Pendlebury, M. Barroso, K. Sivula, M. Gratzel, J.R. Durrant, D.R. Klug, *J. Am. Chem. Soc.*, 2011, **133**, 10134-10140.
72. S. R. Pendlebury, M. Barroso, A. J. Cowan, K. Sivula, J. Tang, M. Grätzel, D. Klug and J. R. Durrant, *Chem. Commun.*, 2011, **47**, 716-718.
73. P. Zubko, S. Gariglio, M. Gabay, P. Ghosez and J. -M. Triscone, *Annu. Rev. Condens. Matter Phys.*, 2011, **2**, 141-165.

74. R. J. Newhouse, H. Wang, J. K. Hensel, D. A. Wheeler, S. Zou and J. Z. Zhang, *J. Phys. Chem. Lett.*, 2011, **2**, 228-235.

This page intentionally left blank.

3 Engineering impurity distributions in photoelectrodes for solar water oxidation

3.1 Abstract for Section 3

This section introduces and experimentally verifies the conceptual framework for the design of solar water oxidation photoelectrodes based on the spatially inhomogeneous doping of metal oxide nanostructures. Optical absorption and electronic conduction can be decoupled and optimized by spatially segregating the functional impurity species that facilitate their associated physical processes. The nanostructure regions possess functional specificity that is established by their chemical composition and three-dimensional geometry, which includes volume, orientation with respect to the direction of light propagation, as well as proximity to the semiconductor-liquid interface. Experimental results indicate optical absorption at visible wavelengths and the related water oxidation conversion efficiencies can be enhanced by physically distributing absorbing crystallites along the direction of light propagation while maintaining their close proximity to the oxide-water interface. An optimization pathway based on these results, analogous to the well-known optimization procedures for excitonic photovoltaic devices, is suggested.

The distinction between electricity and fuel use in analyses of global power consumption statistics highlights the critical importance of establishing efficient synthesis techniques for solar fuels—those chemicals whose bond energies are obtained through conversion processes driven by solar energy.¹ Photoelectrochemical (PEC) processes show potential for the production of solar fuels because of their demonstrated versatility in facilitating optoelectronic and chemical conversion processes.² Tandem PEC-photovoltaic modular configurations for the generation of hydrogen from water and sunlight (solar water splitting) provide an opportunity to develop a low-cost and efficient energy conversion scheme.^{3,4} The critical component in devices of this type is the PEC photoelectrode, which must be optically absorptive, chemically stable, and possess the required electronic band alignment with the electrochemical scale for its charge carriers to have sufficient potential to drive the hydrogen and oxygen evolution reactions. After many decades of investigation, the primary technological obstacle remains the development of photoelectrode structures capable of efficient conversion of light with visible frequencies, which is abundant in the solar spectrum.⁵ Metal oxides represent one of the few material classes that can be made photoactive and remain stable to perform the required functions.^{6,7} This report presents a strategy to decouple the crucial optical absorption and electronic transport processes required for operation of metal oxide photoelectrodes by spatially segregating the functional impurity concentrations that facilitate their associated physical processes.

One technique to sensitize metal oxides to visible light is to introduce dopants that are associated with visible-light-active electronic transitions.^{8,9} If dopant species are introduced in low concentration, below the substitutional limit in the host oxide lattice, optical spectroscopy measurements of films and particle suspensions (typical photoelectrode and photocatalyst configurations) commonly indicate weak shoulders associated with dopant-induced light absorption relative to the host's band-edge absorption.¹⁰ This observation relates to the comparably lower density of states of absorbing impurity levels within the host oxide band

structure: because the solubilities of many dopants of interest are restricted to a few atomic percent,⁸ for nearly equivalent cross sections dopant-induced absorption is expected to be an inherently weaker process than absorption directly affected by the host oxide band structure. Heavily doping beyond the substitutional limit will assist further in sensitization, but with an associated sacrifice of crystallographic order in the surrounding lattice.

Consequently, in order to achieve optical thickness at these weakly absorbing wavelengths, the path length within the electrode structure must be increased, which for conventional film-based electrodes requires the fabrication of physically thick structures. The use of thick films, however, is problematic because of the generally poor transport of carriers in metal oxides, and especially carriers associated with isolated impurity states. The disparity between absorption lengths and transports lengths in oxide materials of interest for this application is addressed generally in the growing literature dedicated to the use of nanotechnologies for solar PEC hydrogen generation.⁷

These observations suggest that doping traditional metal oxide photoelectrodes presents the unacceptable situation where many free carriers generated by visible light excitations recombine before reaching the rear contact or reacting electrochemically at the oxide-liquid interface. Consequently, a viable strategy to enhance the conversion efficiencies of doped metal oxide-based photoelectrodes should be to decouple the optical absorption and electronic conduction processes that occur during their operation. In order to accomplish this, the electrode architecture must be designed such that the associated physical phenomena are segregated, while maintaining spatial register among the facilitating structure regions.

Fortunately, the technological implementation of weakly absorptive materials with poor charge transport properties has been comprehensively addressed in the various designs for metal-oxide-containing excitonic photovoltaic devices.¹¹ In these devices, organic dyes¹² or semiconductor nanocrystals¹³ are intimately contacted with media whose operational purpose is to selectively accept (or separate) and transport photogenerated charges for collection in an external circuit. This configuration has also been applied toward the photoelectrochemical generation of hydrogen in electrolytes containing sacrificial reagents to considerable success.¹⁴ If the concept is applied toward the fabrication of metal oxide photoelectrodes for water splitting an analogy can be drawn between the sensitizer phase and a doped, visible-light-active oxide crystal, in that both of these materials are optically absorptive in the spectral range of interest but efficiently transport charges only over short physical distances. Deposition onto nanostructured substrates permits the use of absorber layers with small physical thickness but large optical thickness (as realized for example in extremely-thin-absorber photovoltaic cells¹⁵ and α -Fe₂O₃ photoanodes^{16,17}). If the substrate is of the same character as the sensitizer phase, the conceptual outcome of this application is a single-phase, oxide nanostructure that is inhomogeneously doped to perform the optoelectronic conversion processes relevant to the oxidation of water using solar energy. The isostructural nature of the absorbing and conducting regions in this case has the potential to yield low concentrations of interface recombination centers, which has significant consequences on the overall conversion efficiencies of PEC devices.

The concept is presently demonstrated with ZnO nanostructures doped in core regions with shallow Al donor levels for enhanced electronic conduction and in the near-surface volume with intragap Ni impurity states for increased optical absorption. However, the strategy is quite

general and can be applied to numerous oxides and impurities; additional experiments were conducted with photoactive nitrogen impurities in place of nickel, with similar, albeit less-pronounced, PEC performance enhancements evident. Figure 9 provides electron microscopy images of the complete structures as well as a schematic of the proposed operating mechanisms within the oxide structure described later in this report; its composition is discussed in detail below. The change in morphology upon introduction of ZnO:Ni is shown in Figure 14.

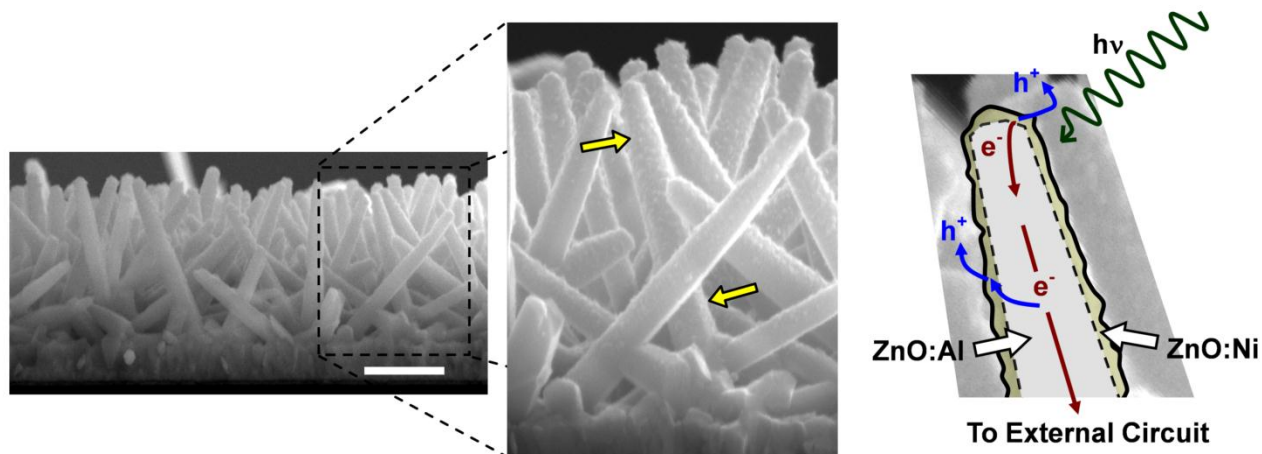


Figure 9. Scanning electron microscopy images of ZnO nanostructure arrays, with yellow arrows highlighting doped crystallites distributed approximately $1.5 \mu\text{m}$ along the direction of light propagation. White scale bar indicates $1 \mu\text{m}$. Right hand side provides a schematic of idealized operating mechanisms overlaid onto the tip of an individual nanostructure.

Substitutional Al is a shallow donor in the ZnO nanocrystal lattice and is associated with large increases electronic conductivity, which results from an order of magnitude increase in carrier concentration.¹⁸ The ionization energy of Al states has been measured to be approximately 90 meV.¹⁹ It is therefore identified as a suitable dopant to facilitate enhanced electronic conduction to the rear contact during PEC operation.

Visible light sensitization on the other hand involves the introduction of impurity states deeper within the bandgap of ZnO. Substitutional impurities on the cation site can be used to functionally sensitize ZnO crystals if they introduce impurity levels or bands that are situated at potentials meeting the thermodynamic requirement for water oxidation. The requirement is met by a number of transition metal impurities; the mechanism by which these impurities sensitize ZnO to visible wavelengths will be discussed later in this report.

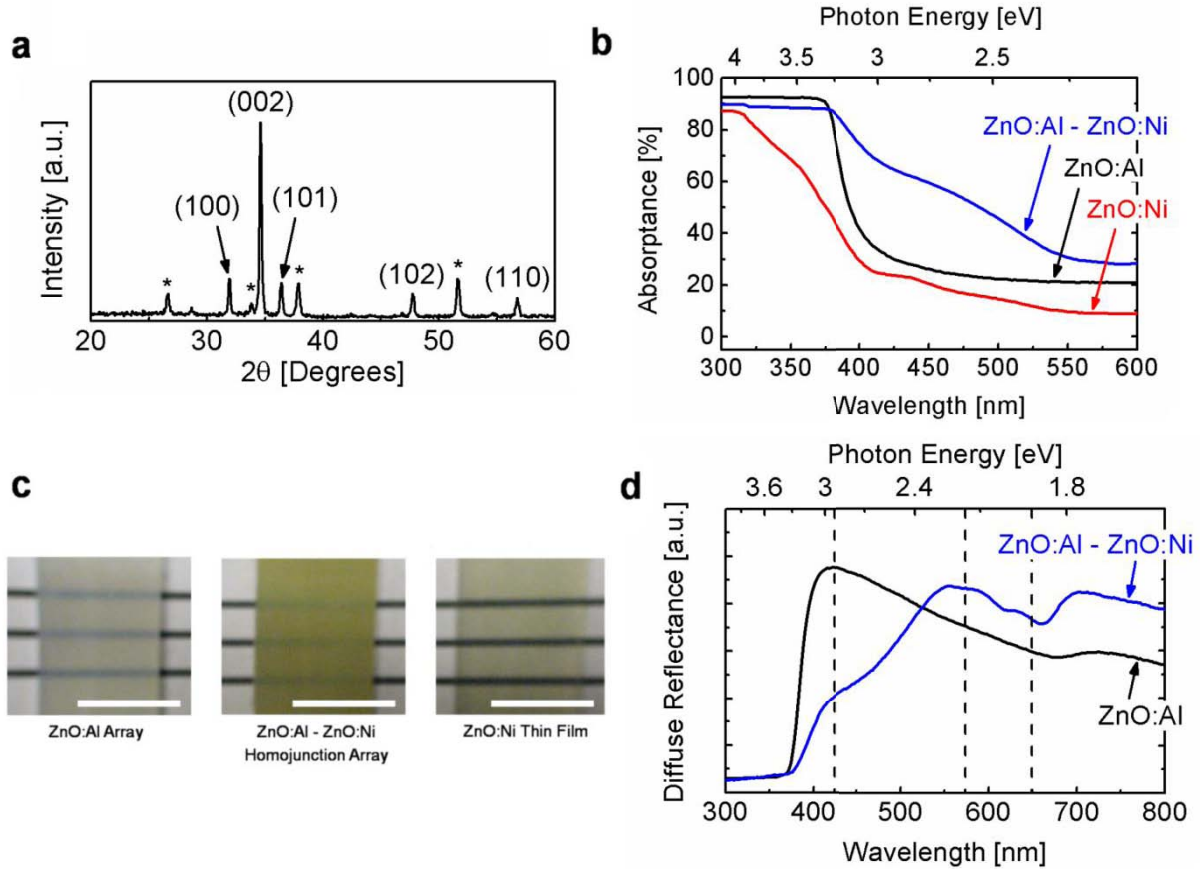


Figure 10. Structural and optical characterization of ZnO nanostructure arrays with and without ZnO:Ni modification: (a) X-ray diffraction pattern of final ZnO nanostructure array. Hexagonal ZnO (wurtzite) is indexed; tetragonal SnO₂ (cassiterite) substrate peaks indicated by *. (b) Absorbance spectra ($A_\lambda = 100 - T_\lambda - R_\lambda$) of ZnO/FTO/glass structures. (c) Photographs of ZnO:Al array (left), ZnO:Al – ZnO:Ni array (middle), and ZnO:Ni thin film (right). White scale bars indicate 1 cm. (d) Diffuse reflectance spectra; dashed lines electronic transitions established in the literature for Ni(II) with tetrahedral symmetry in the ZnO lattice (see main text for details).

An x-ray diffraction pattern (Figure 10a) after fabrication indicates the presence of hexagonal ZnO and the tetragonal SnO₂ substrate (FTO). The ZnO is highly (002)-textured, which results from the c-axis alignment of nanostructures normal to the substrate. The small unlabeled peaks around 26° and 56° were present in all ZnO samples regardless of dopant composition, and are tentatively attributed to a contamination artifact from the fabrication procedure.

The optical absorbance spectra of ZnO nanostructure arrays deposited onto FTO substrates with and without the introduction of crystallites doped with Ni are shown in Figure 10b. The absorption features beyond 400 nm are associated with a change in sample color from transparent-white to green (see sample photographs in Figure 10c), which is consistent with previous reports.²⁰ A reference ZnO:Ni thin film, deposited under identical conditions directly

onto the FTO substrate, is also included in Figures 10b and 10c. Comparison of these optical properties highlights the dramatic increase in optical thickness at visible wavelengths that is associated with the nanostructured homojunction architecture.

The broad absorption features at long wavelengths overlap with transitions associated with tetrahedrally coordinated Ni(II) in the ZnO lattice. Examination of the diffuse reflectance spectra for ZnO:Al and ZnO:Al-ZnO:Ni on FTO/glass substrates in Figure 10d provides additional resolution for these transitions. The dashed lines in this figure indicate the known electronic transitions associated with Ni(II) with tetrahedral symmetry (the transitions at 2.14 eV and 1.89 eV correspond to ${}^3T_1(F) \rightarrow {}^3T_1(P)$ for $Ni_{tet}^{2+} : 3d^8$).^{20,21} The plot indicates reflectance features at these wavelengths that are introduced along with Ni-doped ZnO crystallites, which suggest a tetrahedral coordination of Ni(II).

Photoelectrochemical characterization of the ZnO/FTO electrodes in aqueous 0.5 M Na₂SO₄ provides confirmation of the concept's successful application toward visible-light-driven solar water splitting. Current-potential curves (Figure 11a) indicate a monotonic photocurrent increase with applied anodic potential until the onset of dark current, which suggests effective charge separation at the semiconductor-liquid junction.²² Insertion of a UV filter in the optical path, which eliminates wavelengths below 410 nm, causes a moderate decrease in photocurrent response. The magnitude of the contribution of UV-driven photoactivity to total activity is explained by the comparably small UV photon flux available in solar (simulated) light (~5% of spectral intensity). Amperometric (current-time) measurements with application of color filters shown in Figure 11b indicate the portion of total photocurrent driven by visible light. In these conditions approximately 44% of total photocurrent originates from wavelengths beyond 410 nm; 4.4% originates from beyond 510 nm. Similar analyses of ZnO electrodes without Ni indicate the photocurrent is almost completely UV-driven (see Figure 18).

The incident photon conversion efficiency (*IPCE*) at visible wavelengths for front-side irradiation and with +1 V applied versus a Pt counter electrode is presented in Figure 11c. There is a marked decrease (*ca.* 4 times) of UV photoactivity upon addition of ZnO:Ni species (see Figure 17), which can be understood by observation that all photoholes originating from UV excitation must pass through impure visible-light-active crystals at the ZnO-water interface. Efficiency losses of this type can be minimized through the general optimization of electrode architecture, as discussed below.

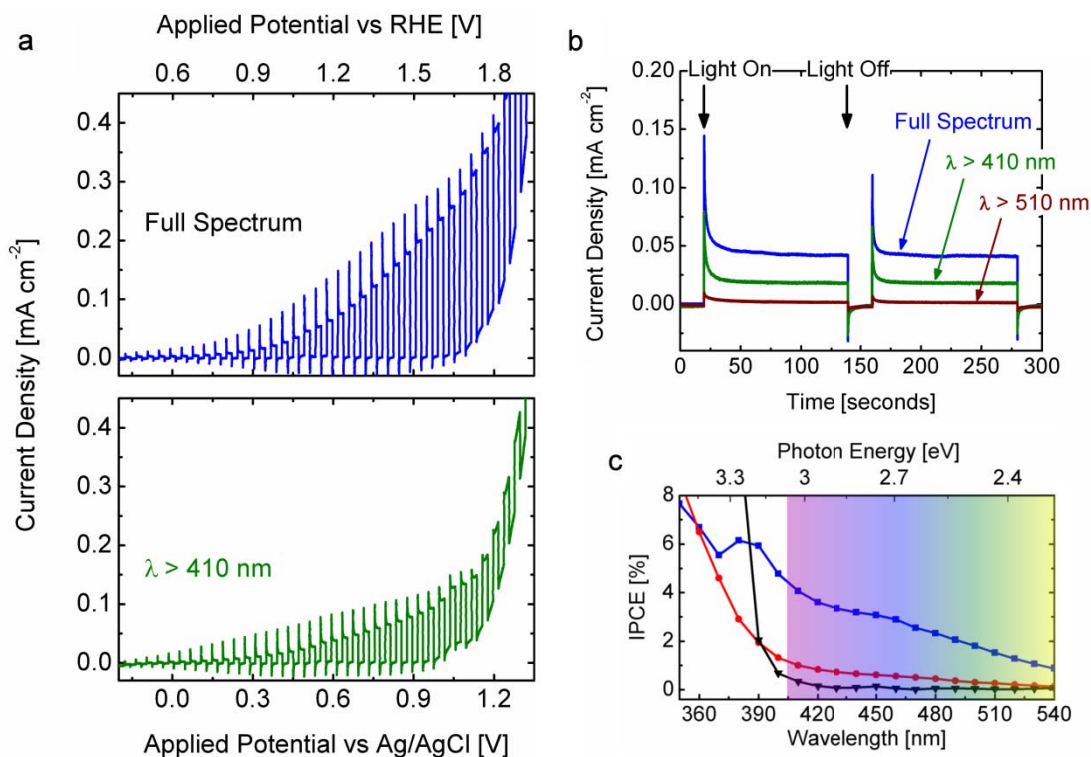


Figure 11. Photoelectrochemical characterization of ZnO electrodes in 0.5 M Na_2SO_4 : (a) Current density-potential curve under chopped AM 1.5G-filtered 100 mW cm^{-2} solar-simulated irradiation with and without application of a UV filter. (b) Amperometric (current-time) measurement at 0.6 V versus Ag/AgCl with chopped AM 1.5G-filtered 100 mW cm^{-2} irradiation, with application of wavelength filters. (c) Incident photon conversion efficiency at visible wavelengths for ZnO:Al-ZnO:Ni homojunction array (blue squares), ZnO:Ni thin film (red circles), and ZnO:Al nanorod array (black triangles), with +1 V applied versus a Pt counter electrode.

To investigate the effect of the homojunction architecture on visible-light-driven water oxidation efficiency, the IPCE spectrum of a dense ZnO:Ni thin film deposited under identical conditions is compared to the nanostructured homojunction array. Presented in Figure 11c, these data indicate that approximately a three-fold enhancement in conversion efficiencies for solar-abundant visible wavelengths is achieved by distributing the absorptive species normal to the substrate and along the direction of light propagation. It is determined that the design effectively shifts the spectral photocurrent response of ZnO electrodes toward lower energies abundant in the solar spectrum.

D. Fichou *et al.* examined the spectral photocurrent contribution toward water oxidation of isovalent Mn^{2+} , Co^{2+} , and Ni^{2+} dopants in ZnO polycrystalline photoanodes.²⁰ It was suggested that visible light photoactivity originated from $d-d$ transitions within the dopant ion, with subsequent charge transfer into the ZnO band structure. In this interpretation, photoelectrons originating from impurity $3d^n$ excitations were transferred to the ZnO conduction band (Zn $4s^0$ orbitals); holes were transported to the ZnO-electrolyte interface in a defect band and were electrochemically active in a buffered Na_2SO_4 solution.

More recently however, work from D. R. Gamelin and coworkers²³⁻²⁶ has unambiguously determined that charge transfer states are required to generate observable photocurrents associated with transition metal dopants in ZnO. Based on these previous analyses of ZnO:Co²⁴ and ZnO:Ni,²³ excitations with wavelengths near 430 nm can be assigned to an acceptor-type ionization, where an electron is promoted to the dopant *d*-shell orbitals from ZnO-based donor orbitals of the valence band.²⁴ If the ZnO lattice is considered a ligand of the dopant ion, these transitions fit the general description of ligand-to-metal charge transfer transitions. The excited state of the charge transfer transition in this case is a valence band hole Coulombically bound to a Ni⁺ dopant ion. This can be deduced from the numerous previous analyses of isovalent transition metal dopants in ZnO and other II-VI semiconductor lattices.^{23,24,26,27} These references suggest the excitation can be described as



The bound carrier generated from this excitation should possess a hydrogen-like wavefunction²³ and a potentially large orbital radius,²⁷ but one which is reduced relative to a free hole. In the context of this assignment, it is clear that the efficient utilization of valence band charge transfer transitions for solar water oxidation will require the use of thin doped regions that are located in close proximity to the electrolyte.

Based on these optical and photoelectrochemical data and the literature cited in this article, some conclusions can be drawn regarding the electronic band structures of the inhomogeneously doped nanostructures. The carrier transfer under irradiation, confirmed by the above photoelectrochemical characterization, was depicted schematically in the right hand side of Figure 9. The band diagram in Figure 12 reflects the theoretical understanding of photoanode operation established in the literature²⁸ but is augmented by the literature-derived electronic states matching the profiles in the structures.

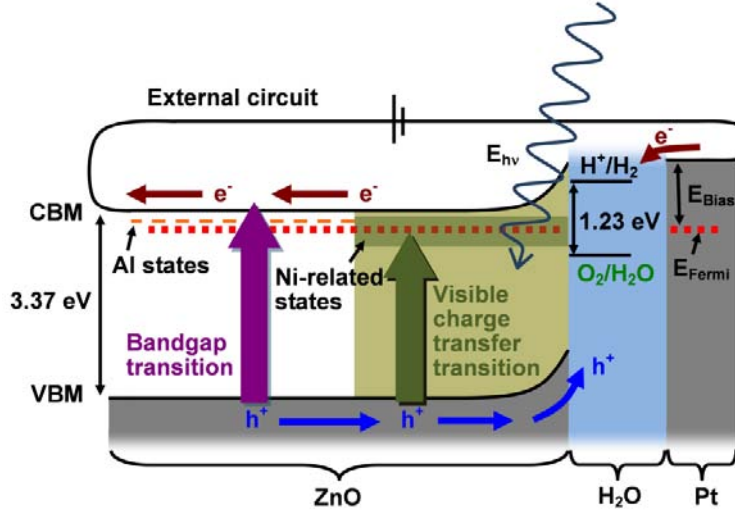


Figure 12. Idealized energetics of the functional homojunction nanostructures demonstrated in this study. Note that surface/interface and other defect states are likely to be present but are omitted in the diagram as they were not studied experimentally. Relative positions of electronic states are schematic but based on literature values (see main text).

In order to investigate the nature of the observed efficiency enhancements at visible wavelengths, the internal quantum efficiency, or absorbed photon conversion efficiency, of the samples were calculated. These efficiencies were calculated through the following equations:

$$T_{measured} = T_1 \times T_2 \times \dots \times T_n \quad (2)$$

$$T_{\lambda, film} = \frac{T_{\lambda, measured}}{T_{\lambda, substrate}} \quad (3)$$

$$A_{\lambda} = \ln(T_{\lambda, film}) \quad (4)$$

$$LHE_{\lambda} = 1 - e^{-A_{\lambda}} \quad (5)$$

$$APCE_{\lambda} = \frac{IPCE_{\lambda}}{LHE_{\lambda}} \quad (6)$$

Where T_n is the transmittance of a component in the layered structure, $T_{\lambda, film}$ is the transmittance of the film, corrected for the substrate as from equations 2 and 3, A_{λ} is the absorbance, LHE_{λ} is the light harvesting efficiency, and $APCE_{\lambda}$ is the absorbed photon conversion efficiency,. The LHE and $APCE$ as calculated from the above equations are plotted in Figure 13. The magnitudes of the $APCE$ values increase dramatically for wavelengths where there is little light absorption, which results in oscillations in the curves corresponding to those in the LHE spectra.

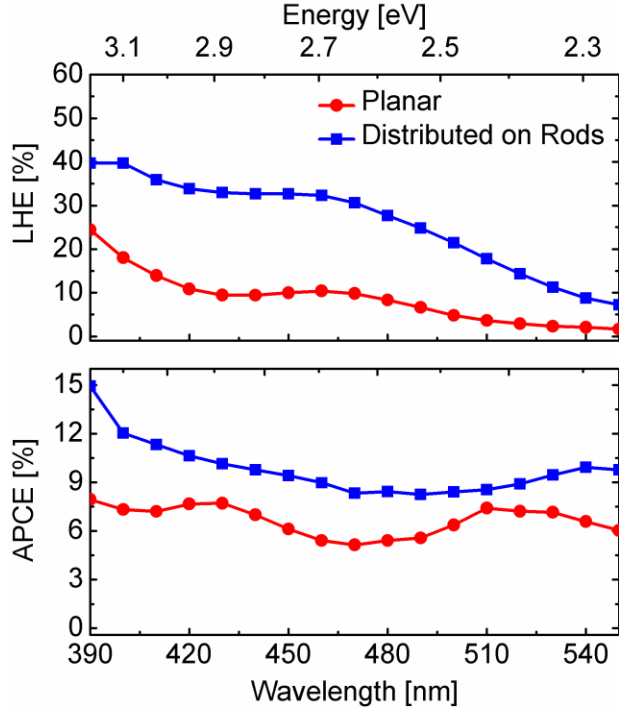


Figure 13. Light harvesting efficiency (top panel) and absorbed photon conversion efficiency (bottom panel) as defined in the main text. Blue squares correspond to efficiencies when ZnO:Ni is distributed on nanorods along the direction of light propagation; red circles correspond to those for a planar ZnO:Ni thin film.

These curves indicate that both the *LHE* and *APCE* at visible wavelengths are increased by distributing ZnO:Ni vertically along the direction of light propagation. The variation in the *APCE* values over this spectral range may indicate differences in intrinsic escape probabilities for photogenerated electrons and holes.²⁴ Longer wavelength excitations may correspond to alternative excitations, such as those related to metal-to-ligand charge transfer transitions, which have different branching ratios for charge separation in their excited states. The transitions could be sensitized by an optical absorption band near 2.9 eV, which would tend to flatten the *IPCE* curve relative to the *APCE* curve. In Figure 13, the oscillations in *APCE* are present in both planar and distributed configurations, which suggests they are related to the electronic structure of the material itself. More in-depth analyses of the material's electronic structure would be required to elucidate the nature of these transitions.

This observation of enhanced *LHE* and *APCE* provides confirmation of the proposed benefits of the homojunction architecture discussed above: greater *LHE* suggests an enhancement in optical absorption and greater *APCE* at visible wavelengths suggests an enhancement in charge separation. Because the thickness of the photoactive layer is reduced by distributing species over a larger surface area substrate, the design facilitates shorter carrier transport path lengths to phases where carrier extraction occurs. This result may also suggest that electrons excited from

charge transfer transitions within the ZnO bandstructure are more easily transferred to the ZnO:Al phase than to the SnO₂:F substrate.

In an optimized photoelectrode, the dopant profiles within the structures should be tailored to maximize conversion efficiency, which depends on, among other quantities, the free electron mobility and concentration, minority carrier (hole) transport length, and extinction coefficient. The metal oxide's feature dimensions should be constructed to maximize both the spectral overlap of optical absorption with the terrestrial solar flux and quantity of photogenerated minority carriers reaching the oxide-water interface.

As part of an initial effort toward design optimization, the optical functions of a ZnO:Ni thin film were approximated by a combined ellipsometry-reflectometry technique (see Supporting Information for details), the results of which are consistent with previous measurements of metal-doped ZnO films.²⁹ These analyses accurately determine the complex refractive index and associated spectral absorption coefficient of the film. The light penetration depths determined by this spectral quantity (Figure 16) suggest that the optimal structure dimension in the direction of light propagation is on the order of several micrometers, which could be reduced by accounting for the significant light scattering effects associated with irradiation of nanowire arrays.³⁰

Here again a close analogy can be drawn to the design of dye-sensitized solar cells, which require dye molecule adsorption over several micrometers of porous structure to achieve optical thickness.¹² Careful analyses of SEM images such as those in Figure 9 indicate the absorptive crystallites are distributed for as long as 1.5 μm along the direction of light penetration. The demonstrated efficiency enhancement in Figure 11c is conceptually similar to the dramatic enhancement evident in dye-sensitized solar cells when planar TiO₂ dye adsorption substrates are replaced with nanostructured TiO₂.³¹ It is suggested that an optimization route for fabrication of efficient homojunction nanostructures of this type is analogous to maximization of dye loading in dye-sensitized solar cells—optimization requires the select doping of the near-surface volume of porous nanostructures over several micrometers.

There is in fact an all (electro)chemical route to the fabrication of metal oxide homojunction nanostructure arrays of the type described above. Chemical growth of ZnO and TiO₂ structures with very large aspect ratios have been reported by various techniques.³²⁻³⁴ In addition, electrochemical deposition has successfully been employed in the literature to obtain conformal deposition of films into deeply-structured substrates.¹⁵ Doped metal oxide films are routinely fabricated by electrodeposition.³⁵ A two-step (electro)chemical process is therefore proposed for the fabrication of high-aspect ratio metal oxide homojunction nanostructure arrays. Such a process is expected to accomplish fabrication at low temperatures, which suggests compatibility with low-cost and flexible substrates. Experiments of this type are currently underway in the authors' laboratories. Additional future work includes the in-depth analysis of the long-term stability of the dopants and their concentration profiles under operating conditions, a theoretical prediction of the optimal electrode three-dimensional geometry based on known material properties, as well as an analysis of optimal material systems suitable for this technique.

This report has introduced and experimentally verified the conceptual framework for the design of solar water oxidation photoelectrodes based on the spatially inhomogeneous doping of metal

oxide nanostructures. Optical absorption and electronic conduction can be decoupled and optimized by spatially segregating the functional impurity species that facilitate their associated physical processes. The nanostructure regions possess functional specificity that is established by their chemical composition and three-dimensional geometry, which includes volume, orientation with respect to the direction of light propagation, as well as proximity to the semiconductor-liquid interface. Experimental results indicate optical absorption at visible wavelengths and the related water oxidation conversion efficiencies can be enhanced by physically distributing absorbing crystallites along the direction of light propagation while maintaining their close proximity to the oxide-water interface. An optimization pathway based on these results, analogous to the well-known optimization procedures for excitonic photovoltaic devices, has been suggested.

3.2 Experimental details

The nanostructures were fabricated through a combination of electrochemical deposition and physical vapor deposition. Physical, optical, and photoelectrochemical characterization were performed by standard techniques. Experimental details are provided in the Supporting Information.

3.3 Supporting information

3.3.1 Morphology

Top-down scanning electron microscopy (SEM) images of the rod arrays before and after modification with ZnO:Ni are provided in Figure 14.

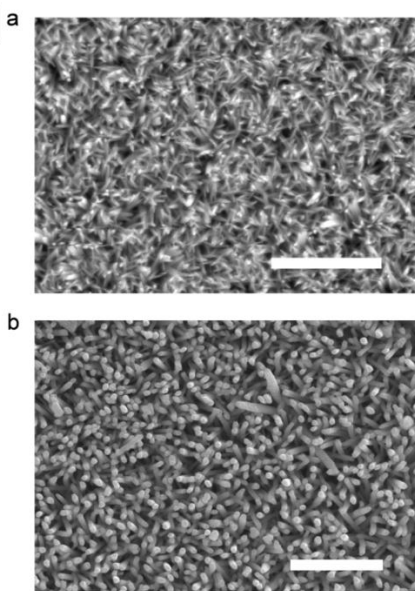


Figure 14. Top-down SEM images of ZnO nanorod arrays before (a) and after (b) modification with ZnO:Ni. White scale bars indicate 2.5 μm.

3.3.2 Experimental details

3.3.2.1 Fabrication

Al-doped ZnO nanorod arrays were fabricated by electrochemical deposition in a three-electrode cell employing a Pt wire counter electrode, silver/silver chloride (Ag/AgCl) reference electrode (Pine Instruments; in 4 M KCl; separated from the electrolyte by a porous frit), and FTO (Pilkington; TEC7) working electrode contacted to a Cu wire with conductive Ag paste. Before deposition, FTO/glass substrates were sequentially sonicated in acetone, ethanol, and water for 15 minutes each. Deposition occurred for 0.5-1hr at 90 °C and at -0.9 V vs. Ag/AgCl in an aqueous (18.1 M Ω -cm water) electrolyte containing 1-6 mM zinc nitrate hexahydrate (Zn(NO₃)₆H₂O; 98%; Aldrich) and methenamine (C₆H₁₂N₄; Mallinckrodt Chemicals) as described by Vayssieres,³⁶ and 1-5 μ M aluminum chloride (AlCl₃; 99.999%; Aldrich).

The arrays were modified by species generated from the pulsed laser ablation of pressed polycrystalline targets in O₂ and N₂ ambients. ZnO and NiO targets were selectively ablated in the presence of oxygen (or mixture of oxygen and nitrogen for ZnO:N deposition) and species from the resulting plasma were deposited onto the ZnO:Al/FTO samples as prepared by electrochemical deposition. The pressure during deposition was 3-5 mtorr as measured by a pirani pressure gauge mounted on the chamber. The samples presented in the main text were maintained at 200 °C, using a resistive heater and a thermocouple probe embedded in the substrate holder. The laser fluence at the target surface (pulse energy, spot size) and target-substrate distance were selected such that a uniform film could be deposited over several square centimeters.

3.3.2.2 Physical characterization

Scanning electron microscopy (SEM) images were obtained with a Hitachi environmental field emission scanning electron microscope (Model S-4300SE/N) operating in secondary electron detection mode.

Spectral transmittance and diffuse reflectance measurements were taken on the ZnO/FTO/glass samples with a Perkin Elmer Lambda Spectrophotometer fitted with an integrating sphere at a wavelength interval of 2 nm. The sample was irradiated at the front surface. The spectral absorbance was obtained by solution of the equation $A_\lambda = 100 - R_\lambda - T_\lambda$, and no correction was made for the substrate.

X-ray diffraction (XRD) measurements were performed on a Siemens D5000 diffractometer with Cu K α radiation.

3.3.2.3 Photoelectrochemical characterization

All electrolytes were prepared with 18.1 M Ω -cm water. The electrolyte for all PEC measurements was prepared as 0.5 M sodium sulfate (Na₂SO₄; > 99 % ACS grade; Sigma Aldrich); pH \approx 6.8.

Photoelectrochemical measurements were acquired in an open pyrex cell fitted with a quartz window. A 1 cm² masked-off, sealed area of the sample was irradiated with a 300 W Xe lamp solar simulator with adjustable power settings through an AM 1.5G filter (Oriel; 81092). The light intensity at the sample location in the photoelectrochemical cell was 100 mW cm⁻² as measured by a power detector (Newport; 70284). No correction was made for the optical absorption of the ~ 4 cm of electrolyte between the quartz window and sample location. A potentiostat (Pine Instruments Bipotentiostat) was used to measure electrochemical data in a 3-electrode setup using a Ag/AgCl reference electrode (Pine Instruments) and a coiled Pt wire counter electrode. The reversible hydrogen electrode (RHE) potential was calculated as $E_{\text{RHE}} = E_{\text{Ag/AgCl}} + 0.1976 + 0.057 \cdot \text{pH}$. N₂ gas was continuously bubbled in solution and directly over the Pt counter electrode before and during the experiment to remove any dissolved O₂ and therefore suppress the reduction of O₂ at the counter electrode. For current-potential measurements, the potential scan was anodic (in the positive direction) and at a rate of 5 mV s⁻¹, with the light mechanically chopped at 0.2 Hz. For the UV filters employed, the transmission of light below the cut-off is below ~1%; ~10% of intensity is absorbed for wavelengths above the cut-offs.

For *IPCE* measurements, +1 V was applied versus a Pt foil located 1 cm from the irradiated portion of the sample. No correction was made for ohmic losses in the electrolyte. N₂ was bubbled in solution before measurements but experimental constraints did not permit bubbling during measurement. *IPCE* measurements were obtained on a quantum efficiency measurement system employing a Xe lamp, monochromator (5 nm FWHM, 10 nm interval), and light chopper (5 Hz), with a portion of the beam diverted to a photodiode. Data points represent averages of 6 measurements of 5 second sampling periods per wavelength. The system was calibrated before measurement using a NIST-calibrated Si photodiode.

3.3.3 Ellipsometry-reflectometry

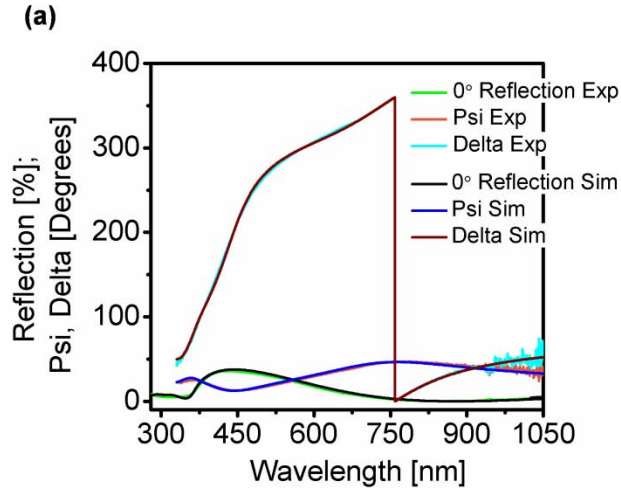
The optical functions of the ZnO:Ni discussed in the main text were approximated by a combined ellipsometry-reflectometry technique performed with a commercial thin film metrology system (Scientific Computing International; FilmTek Par 3000 SE). During deposition of ZnO:Ni a small (001) Si substrate was mounted approximately 1 cm from the area later probed by photoelectrochemical (PEC) measurements. The ellipsometric parameters psi and delta were measured on this sample at 70° incidence and over the wavelength range 350-1050 nm at 0.25 nm intervals. The specular reflection spectrum was recorded at 0° (normal) incidence over the range 280 nm to 1050 nm at 0.25 nm intervals. The measured quantities are indicated in Figure 15a, as labeled in the figure legend.

The Tauc-Lorentz relation formulated by Jellison and coworkers³⁷ was used over the entire wavelength range to model the optical functions of the ZnO/Si structure. This dispersion relation forces the extinction coefficient $k(E)$ to be zero at photon energies less than the optical gap and permits a reduction in $k(E)$ as $E \rightarrow \infty$. However, the parameterization only describes interband transitions and cannot resolve Urbach tails or isolated defect transitions associated with impurity levels.³⁷ Strictly speaking the dielectric function of ZnO has differing extraordinary and ordinary components. As a first approximation, this analysis assumes the optical properties are isotropic and produces *effective* optical functions. This technique has been previously applied to similar material systems.³⁸

The Bruggeman EMA relation³⁹ was used to model the surface region with mixed dielectric functions. A surface roughness layer was modeled as a 50 % - 50 % mixture of the ZnO layer and void space (air). The native oxide layer on the Si substrate was modeled using the Cauchy relations⁴⁰ with literature values included in the software package. The structure used for simulation with labeled thicknesses determined by the regression analysis is summarized in Figure 15b. A scanning electron microscopy (SEM) image of the ZnO/Si structure's cross section is provided in Figure 15c, which is consistent with the proposed model.

The simultaneous fitting of polarization-dependent reflections at two angles is expected to provide a high degree of accuracy for determination of thicknesses and complex refractive indices of multi-layer structures, and the combined technique assists in avoidance of multiple solutions. The measurement simultaneously probes intensity (reflectometry) and polarization changes (ellipsometry) in reflected light.

The simulated quantities based on this analysis are indicated in Figure 15a. The analysis resulted in a close correlation among experimental and simulated values, yielding a correlation coefficient of $R^2 = 0.9996$. Attempts to add additional physical accuracy through the introduction of additional oscillators and inter-mixing among layers resulted in unacceptable standard errors associated with their fitting. The parameterizations are presented below in equations 1-6 and Tables 2 and 3.



(b)

50% ZnO – 50% Void	19.27 ± 0.30 nm
ZnO	105.75 ± 0.47 nm
SiO ₂	1.23 ± 0.36 nm
Si	

(c)

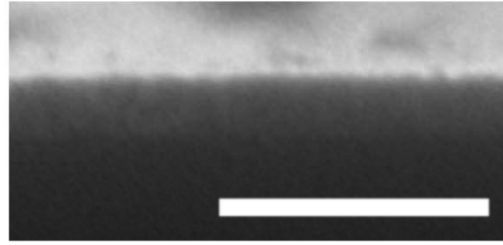


Figure 15. (a) Experimental (Exp) and simulated (Sim) values for reflection measured at normal incidence and ellipsometric parameters psi and delta measured at 70° incidence. (b) Multi-layer structure employed for simulation of ellipsometry-reflectometry data, with thickness and composition quantities determined by the regression analysis. (c) Cross-section SEM image of the ZnO/Si structure. White scale bar indicates 500 nm.

3.3.3.1 SiO₂ layer; Cauchy

$$n_{\lambda} = A_n + \frac{B_n}{\lambda^2} + \frac{C_n}{\lambda^4} \quad (1)$$

$$k_{\lambda} = A_k + \frac{B_k}{\lambda^2} + \frac{C_k}{\lambda^4} \quad (2)$$

Table 2. Values for Cauchy relations used for simulation of SiO₂

Cauchy	
Parameter	Value
A_n	1.447849
B_n	3.41×10^{-3}
C_n	2.05×10^{-5}
A_k	2.86×10^{-19}
B_k	1.23×10^{-19}
C_k	6.56×10^{-21}

$$\varepsilon_2(E) = \sum_j^m \frac{A_j^2 (E_{center})_j \nu (E - E_g)^2}{[E^2 - (E_{center})_j^2]^2} \cdot \frac{1}{E} \quad E > E_g \quad (3)$$

$$\varepsilon_2(E) = 0 \quad E \leq E_g \quad (4)$$

$$\varepsilon_1(E) = \varepsilon_\infty + \frac{2}{\pi} P \int_{E_g}^{\infty} \frac{\xi \varepsilon_2(\xi)}{\xi^2 - E^2} d\xi \quad (5)$$

Table 3. Fitted values for Tauc-Lorentz parameterization and associated standard errors.

Tauc-Lorentz		
Parameter	Value	Standard
ε_∞	3.320	0.009
E_g	1.393	0.061
A	1.818	0.054
E_{center}	3.83	0.011
ν	0.627	0.012

3.3.3.2 Surface layer; Bruggeman EMA

$$\sum_{i=1}^m f_i \frac{\epsilon_i - \epsilon_{eff}}{\epsilon_i + 2\epsilon_{eff}} = 0$$

$$\sum_{i=1}^m f_i = 1 \quad f_1 = 0.5, \quad f_2 = 0.5 \quad (6)$$

Where f_1 is the fraction of ZnO, f_2 is the fraction of void space.

The dielectric function of ZnO:Ni determined by this analysis is presented in Figure 16a. The absorption coefficient, calculated from the modeled extinction coefficient, and its reciprocal, which assuming homogeneity is equal to the mean light penetration depth in the film, is plotted in Figure 16b.

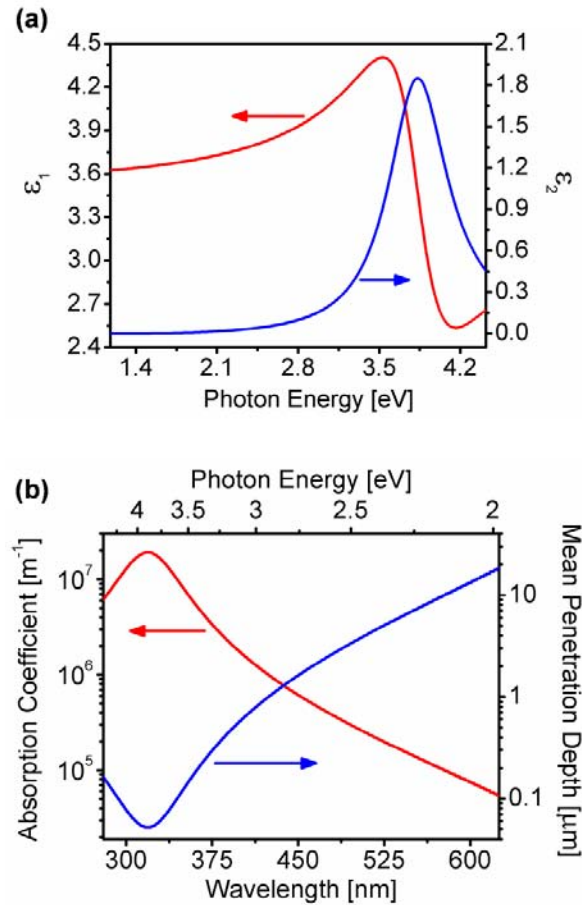


Figure 16. (a) Complex dielectric function, $\epsilon_1 + i\epsilon_2$, as determined by ellipsometry-reflectometry regression analysis. (b) Spectral absorption coefficient and its reciprocal, the mean light penetration depth, for a ZnO:Ni thin film.

3.3.4 Complete IPCE spectra for ZnO:Al-ZnO:Ni system

The complete IPCE spectra for the ZnO:Al and ZnO:Al-ZnO:Ni system described in the main text is provided in Figure 17.

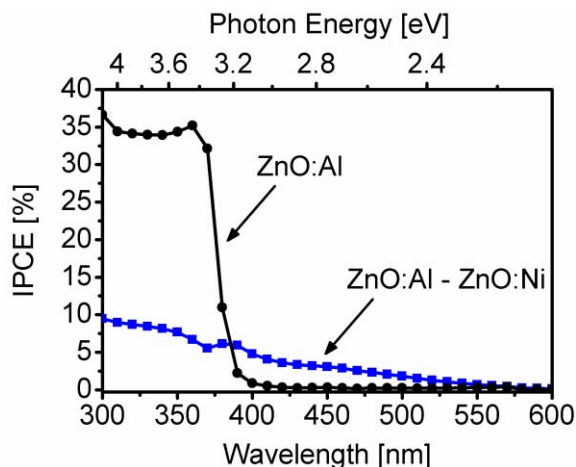


Figure 17. Complete spectra for incident photon conversion efficiencies for front-side irradiation of ZnO:Al – ZnO:Ni photoelectrodes, as described in the main text, in 0.5 M Na₂SO₄ with +1 V applied versus a Pt counter electrode.

3.3.5 Amperometric (current-time) measurement with color filters for ZnO:Al

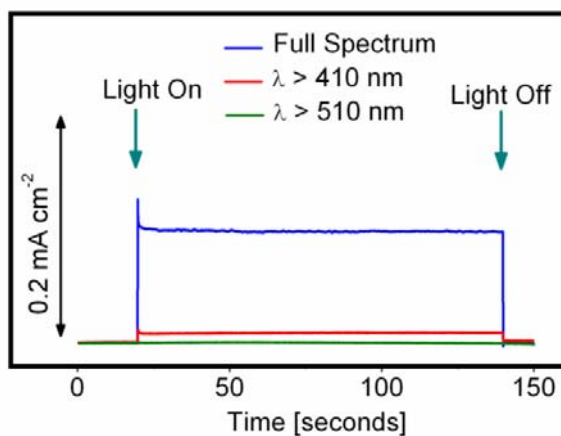


Figure 18. Amperometric current-time measurement for ZnO:Al with chopped AM 1.5G-filtered 100 mW cm⁻² irradiation at 0.6 V vs Ag/AgCl, with application of color filters.

A color-filtered amperometric (current-time) measurement was performed on ZnO:Al without modification with Ni (Figure 18). As expected, the photocurrent is primarily driven by UV excitation, which is only present under full spectrum irradiation. Application of color filters reduces total photoactivity significantly, consistent with IPCE results.

3.4 References

1. N. S. Lewis, D.G. Nocera, *Proc. Nat. Acad. Of Sciences* **2006**, *103*, 15729.
2. N. S. Lewis, *J. Electroanalytical Chem.* **2001**, *508*, 1.
3. J. Augustynski, G. Calzaferri, J. C. Courvoisier, M. Grätzel, in *Proc. of the 11th World Hydrogen Energy Conference* (Eds: T. N. Veziroglu, C. J. Winter, J. P. Baselt, G. Kreysa), Stuttgart, **1996**, 2379.
4. E. L. Miller, R. E. Rocheleau, X. M. Deng, *Int. J. Hydrogen Energy* **2003**, *28*, 615.
5. Walter, M. G., E. L Warren, J. R. McKone, S. W. Boettcher, Q. Mi, E. A. Santori, N. S. Lewis, *Chem. Rev.* **2010**, *110*, 6446.
6. B. D. Alexander, P. J. Kulesza, I. Rutkowska, R. Solarakac, J. Augustynski, *J. Mater. Chem.* **2008**, *18*, 2298.
7. *On Solar Hydrogen & Nanotechnology*, (Ed: L. Vayssieres), Wiley, Singapore, **2009**.
8. M. A. Malati, W. K. Wong, *Surface Technology* **1984**, *22*, 305.
9. K. Rajeshwar, *J Appl. Electrochem.* **2007**, *37*, 765.
10. Z. Zou, J. Ye, K. Sayama, H. Arakawa, *Nature* **2001**, *414*, 625.
11. B. A. Gregg, *J. Phys. Chem. B* **2003**, *107*, 4688.
12. M. Grätzel, *Inorg. Chem.* **2005**, *44*, 6841.
13. A. J. Nozik, *Nano Lett.* **2010**, *10*, 2735.
14. G. Wang, X. Yang, F. Qian, J. Z. Zhang, Y. Li, *Nano Lett.* **2010**, *10*, 1088.
15. K. Ernst, A. Belaidi, R. Könenkamp, *Semicond. Sci. Technol.* **2003**, *18*, 475.
16. J. Glasscock, P. R. F. Barnes, I. C. Plumb, A. Bendavid, P. J. Martin, in *Proc. of SPIE, the International Society for Optical Engineering* (Ed. L. Vayssieres), **2006**, 6340, 63400N.
17. K. Sivula., F. Le Formal, M. Grätzel, *Chem. Mater.* **2009**, *21*, 2862.
18. R. Könenkamp, K. Boedecker, M. C. Lux-Steiner, M. Poschenrieder, F. Zenia, C. Levy-Clement, S. Wagner, *Appl. Phys. Lett.* **2000**, *77*, 2575.
19. H. P. He, Tang, Z. Z. Ye, L. P. Zhu, B. H. Zhao, L. Wang, and X. H. Li, *Appl. Phys. Lett.* **2007**, *90*, 023104.
20. D. Fichou, J. Pouliquen, J. Kossanyi, M. Jakani, G. Campet, J. Claverie, *J. Electroanal. Chem.* **1985**, *188*, 167.
21. H. A. Weakliem, *J. of Chem. Phys.* **1962**, *36*, 2117.
22. X. Yang, A. Wolcott, G. Wang, A. Sob, R. C. Fitzmorris, F. Qian, J. Z. Zhang, Y. Li, *Nano Lett.* **2009**, *9*, 2331.
23. D. A. Schwartz, N. S. Norberg, Q. P. Nguyen, J. M. Parker, D. R. Gamelin, *J. Am. Chem. Soc.* **2003**, *125*, 13205.
24. W. K. Liu, G. Mackay Salley, D. R. Gamelin, *J. Phys. Chem. B* **2005**, *109*, 14486.

25. K. R. Kittilstved, W. K. Liu, D. R. Gamelin, *Nature Mater.* **2006**, 5, 291.
26. C. A. Johnson, T. C. Kaspar, S. A. Chambers, G. Mackay Salley, D. R. Gamelin, *Phys. Rev. B.* **1993**, 48, 8672.
27. J. M. Noras, J. W. Allen, *J. Phys. C.: Solid St. Phys.* **1980**, 13, 3511.
28. A. J. Nozik, R. Memming, *J. Phys. Chem.* **1996**, 100, 13061.
29. A. Mendoza-Galván, C. Trejo-Cruz, J. Lee, D. Bhattacharyya, J. Metson, P. J. Evans, U. Pal, *J. Appl. Phys.* **2006**, 99, 014306.
30. M. D. Kelzenberg, S. W. Boettcher, J. A. Petykiewicz, D. B. Turner-Evans, M. C. Putnam, E. L. Warren, J. M. Spurgeon, R. M. Briggs, N. S. Lewis, H. A. Atwater, *Nature Mater.* **2010**, 9, 239.
31. M. Grätzel, *Nature* **2001**, 414, 338.
32. M. Law, L. E. Greene, J. C. Johnson, R. Saykally, P. Yang, *Nature Mater.* **2005**, 4, 455.
33. X. Feng, K. Shankar, O. K. Varghese, M. Paulose, T. J. Latempa, C. A. Grimes, *Nano Lett.* **2008**, 8, 3781.
34. G. K. Mor, K. Shankar, M. Paulose, O. K. Varghese, C. A. Grimes, *Nano Lett.* **2006**, 6, 215.
35. T. F. Jaramillo, S.-H. Baeck, A. Kleiman-Shwarscstein, K.-S. Choi, G. D. Stucky, E. W. McFarland, *J. Comb. Chem.* **2005**, 7, 264.
36. L. Vayssieres, *Adv. Mat.* **2003**, 15, 464.
37. G. E. Jellison, F. A. Modine, *Appl. Phys. Lett.* **1996**, 69, 371.
38. A. Mendoza-Galván, C. Trejo-Cruz, J. Lee, D. Bhattacharyya, J. Metson, P. J. Evans, U. Pal, *J. of Appl. Phys.* **2006**, 99, 014306.
39. D. A. G. Bruggeman, *Ann. Phys. (Leipzig)* **1935**, 24, 636.
40. H. Fujiwara, in: *Spectroscopic Ellipsometry: Principles and Applications*, (Wiley, West Sussex, UK, **2007**).

4 Electron enrichment in 3d transition metal oxide hetero-nanostructures

4.1 Abstract for Section 4

Direct experimental observation of spontaneous electron enrichment of metal d orbitals in a new transition metal oxide heterostructure with nanoscale dimensionality is reported. Aqueous chemical synthesis and vapor phase deposition are combined to fabricate oriented arrays of high-interfacial-area hetero-nanostructures comprised of titanium oxide and iron oxide nanomaterials. Synchrotron-based soft x-ray spectroscopy techniques with high spectral resolution are utilized to directly probe the titanium and oxygen orbital character of the interfacial region's occupied and unoccupied densities of states. These data demonstrate the interface to possess electrons in Ti $3d$ bands and an emergent degree of orbital hybridization that is absent in parent oxide reference crystals. The carrier dynamics of the hetero-nanostructures are studied by ultrafast transient absorption spectroscopy, which reveals the presence of a dense manifold of states, the relaxations from which exhibit multiple exponential decays whose magnitudes depend on their energetic positions within the electronic structure.

This work involved collaboration with researchers at Stanford University, University of California at Santa Cruz, the Advanced Light Source, and National Institute for Materials Science. Specifically it involved collaboration with Jonathan Bakke and Stacey Bent at Stanford University, Damon Wheeler and Jin Zhang at UC Santa Cruz, Wei-Cheng Wang and Jinghua Guo at the Advanced Light Source, and Lionel Vayssieres at the International Center for Materials NanoArchitectonics, National Institute for Materials Science, Tsukuba, Japan.

The interfaces of oxide heterostructures provide a rich and diverse platform for the discovery and study of unique emergent electronic phenomena, which enables development of new multifunctional materials for several proposed oxide-based electronic device technologies.¹ Oxide interface engineering represents a new materials fabrication strategy, which, given a greater degree of fundamental understanding, could permit the manipulation of the energetic and behavioral specificity of electrons.^{2,3} Here we report the direct experimental observation of electron enrichment of $3d$ orbitals in the interface of a new transition metal oxide heterostructure system based on junctions of titanium oxide and hematite nanomaterials. Further examination of the interface orbital character reveals evidence of an emergent degree of p - d hybridization that is absent from reference parent crystals. These findings and their consequences represent a convergence of nanoscience and oxide interface engineering, two highly influential and technologically promising fields within materials science and chemistry.

Concurrent to the exciting advances¹ in oxide interface engineering, the recent applications of nanoscience to electronic device components, most notably those for solar energy conversion devices, have led to the utilization of a number of physical properties and phenomena that will potentially reduce system fabrication costs and increase overall conversion efficiencies.^{4,5,6} These practices, which are emblematic of third generation solar cells, include the engineering of quantum confinement effects,⁴ plasmonic resonance modes,⁷ intermediate bands,⁸ high specific

surface areas,⁹ and overall optimization of device architectures in relation to operational processes including light absorption and carrier transport.¹⁰ The benefits of hetero-nanostructures, or those structures which contain junctions of dissimilar nanomaterials, can similarly be utilized for a broad range of applications for emerging optoelectronic devices. This includes the suppression of detrimental interfacial back-reactions¹¹ and the separation of photogenerated charges¹² in photovoltaic devices as well as more advanced applications such as the direct manipulation of light-matter-spin interactions for quantum information processing.¹³

In the context provided by these emerging fields, oxide nanostructures, and indeed oxide hetero-nanostructures, show unique potential to address the strict optical and electronic material properties required by the photoactive components of solar energy conversion devices. Photoelectrochemical (PEC) solar technologies in particular stand to benefit from the engineering of oxide hetero-nanostructures, as their enabling photoelectrodes often require great chemical stability as well as a high degree of specialization with respect to optical absorption, charge transfer, and chemical reactivity.⁵ The large oxidative potential resulting from the high ionization energies of most metal oxides is most importantly applied for the photoelectrochemical oxidation of water, a critical step in the sustainable and clean generation of solar fuels such as hydrogen.^{5,14} Here we demonstrate that oxide hetero-nanostructure engineering presents an opportunity to fabricate entirely new materials that possess emergent or unexpected surface and interfacial properties.

4.2 Description of hetero-nanostructure array

The oxide hetero-nanostructure arrays presently investigated were fabricated through a combination of aqueous chemical synthesis¹⁵ and atomic layer deposition^{16,17} (see Experimental Methods for details). Briefly, beta-phase iron(III) oxyhydroxide (β -FeOOH, akaganeite) rod structures were grown directly from an aqueous precursor salt solution by hydrolysis-condensation and heteronucleation onto fluorinated tin(IV) oxide-coated glass ($\text{SnO}_2\text{:F}$, FTO) substrates, as described in reference 18. Annealing (above 450°C) of the vertically aligned β -FeOOH rod arrays resulted in a phase transformation to alpha-phase iron(III) oxide (α -Fe₂O₃, hematite).¹⁸ The α -Fe₂O₃ is organized into bundles of 3-5 nm single crystalline rods whose electrons are quantum-confined in the lateral dimension.¹⁹ Following this, nanocrystalline Ti_xO_y was deposited directly at the α -Fe₂O₃ surface at 150 °C by atomic layer deposition (ALD), a monolayer-by-monolayer growth technique.¹⁶ The resulting structures, which are notated herein as Ti_xO_y-Fe₂O₃, were investigated by synchrotron-based soft x-ray spectroscopy techniques as well as by ultrafast transient absorption spectroscopy. These advanced characterization techniques, which probe the material at atomic length scales and ultrafast time scales, provide a description of the system's band structure and its densities of localized surface and interface states.

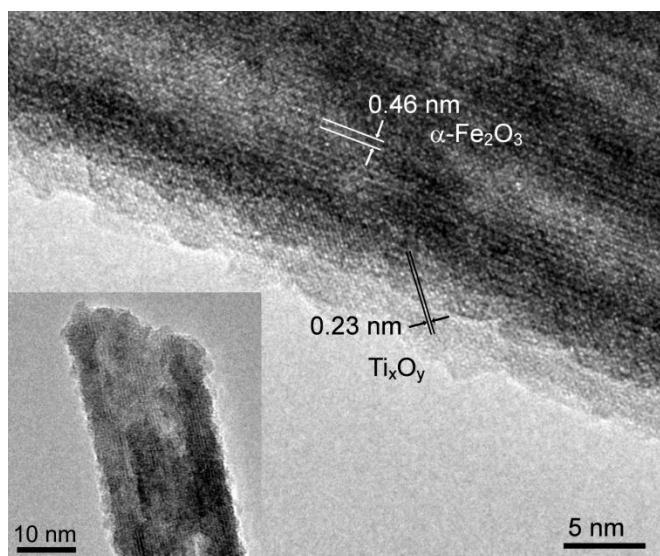


Figure 19. Transmission electron microscopy image of the $\text{Ti}_x\text{O}_y\text{-Fe}_2\text{O}_3$ hetero-nanostructure interface, with lattice fringes evident. Inset provides a lower resolution image of the tip of a complete structure.

Transmission electron microscopy (TEM) images of representative structures are presented in Figure 19. The complete structure displayed in the inset terminates with an uneven surface, which is indicative of bundles of ca. 5 nm diameter rods, as reported previously.^{15,18} The Ti_xO_y structures are visible with lighter contrast on the surface and are distributed conformally along the length of the rod. Heterostructures comprised of $\alpha\text{-Fe}_2\text{O}_3$ and stoichiometric TiO_2 have previously been fabricated, mainly for photoelectrochemical²⁰ and photocatalytic²¹ applications. TiO_2 nanotubes containing $\alpha\text{-Fe}_2\text{O}_3$ crystals, which share a common configuration with the present structures, albeit on longer length scales, have been fabricated with similar applications in mind.²²

By probing with high spectral resolution the unoccupied and occupied densities of states, synchrotron-based x-ray spectroscopy techniques enable detailed analyses of the orbital characteristics of nanomaterials.²³ Of particular interest to the present study is the system's interfacial electronic structure: that is, the character and occupancy of d orbitals at the interface. For this reason results for total electron yield mode, which has a probe depth of ca. 5 nm² and therefore for this structure directly measures the interface, are considered.

4.3 Ti L-edge x-ray absorption

The unoccupied electronic structure of $\text{Ti}_x\text{O}_y\text{-Fe}_2\text{O}_3$ hetero-nanostructures was examined by x-ray absorption spectroscopy (XAS), a technique capable of monitoring a number of important characteristics of the system density of states. For instance, cation charge transfer phenomena across the interface, which can be monitored by XAS,²⁴ will change the overall occupancy of the hetero-nanostructures' metal $3d$ states, which is expected to have significant consequences on the carrier dynamics and thus on the overall performances of optoelectronic devices utilizing transitions to and from such states.

The titanium $L_{II,III}$ -edge absorption spectrum for $Ti_xO_y-Fe_2O_3$ is presented in Figure 20a. Also included in Figure 20a are L-edge absorption spectra measured for three reference titania crystals: anatase TiO_2 ($3d^0$ electronic configuration), Tistarite (corundum) Ti_2O_3 ($3d^1$), and rock salt TiO ($3d^2$). Both the relative spectral intensities and line shapes of these signals contain information relating to the coordination of Ti in the thin surface and interfacial region. The Ti L-edge absorption spectra of titanium oxides have been comprehensively documented.^{25,26,27,28} The two sets of local maxima over this energy range can be assigned to excitations of Ti $2p_{3/2}$ (peaks A and B) and Ti $2p_{1/2}$ (peaks C and D) core levels into empty Ti $3d$ states.²³ These sets of peaks result from the core-hole spin-orbit splitting of the $2p$ levels.²⁷ The ligand field splits the final states into two levels possessing t_{2g} and e_g symmetry;²⁵ the energy difference between these sublevels is related, but not equal, to the field splitting energy.²⁹

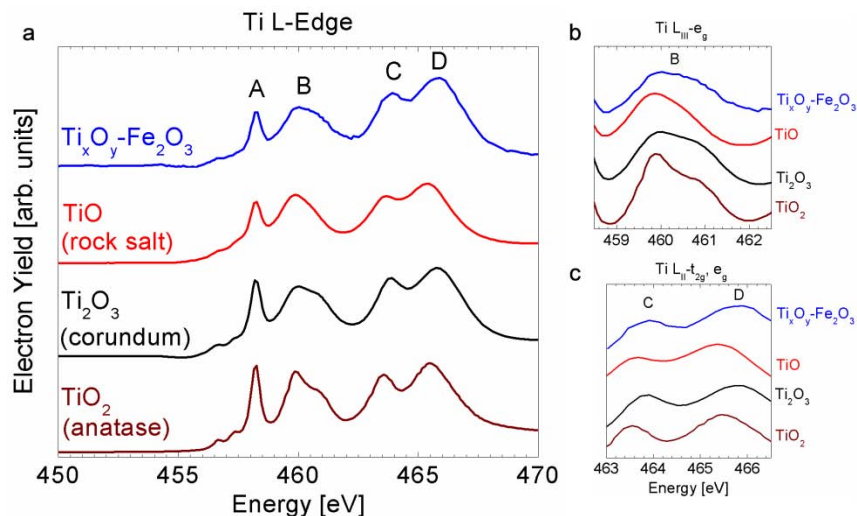


Figure 20. Ti $L_{II,III}$ -edge x-ray absorption spectra for $Ti_xO_y-Fe_2O_3$ and reference TiO (red), Ti_2O_3 (black), and TiO_2 (brown): (a) entire spectral range, (b) resolved spectral range for comparison of $L_{III}-e_g$ peak centered near 460.5 eV (B), and (c) resolved spectral range for comparison of $L_{II}-t_{2g}$ and e_g peaks (C and D). All curves are normalized to their respective intensities at peak D.

First, it is to be noted that the broadening of peak A in Figure 20a, as well as the slight shoulder appearing at the low energy side of this edge, has previously been associated with a reduction in the oxidation state of the cation, and is indeed observed after the controlled reduction of Ti^{4+} surface species on TiO_2 single crystals.³⁰ The slight broadening of peak A and the red-shift of the L-edge absorption onset with respect to that for TiO_2 provides initial evidence of a Ti oxidation state lower than 4+ in $Ti_xO_y-Fe_2O_3$.

In order to understand the nature of the Ti_xO_y structure, it is helpful to consider the characteristics of the $L_{III}-e_g$ peak (peak B), centered near 460.5 eV (Figure 20b). The line shape of the $L_{III}-e_g$ peak is extremely sensitive to the local symmetry of the metal cations,²³ and therefore provides a signature of the bonding environment in the titania layer. In titania reference minerals the line shapes and intensities of the $L_{III}-e_g$ peaks show diversity with respect to the cations' site environments.^{26,31} Generally there are peaks observed between 459 eV and 462 eV,

the origins of which have been considered through several theoretical frameworks.³¹ In anatase TiO₂, the low-energy side of the peak dominates over the high-energy side, whereas in rutile TiO₂ the relative intensities are reversed.²⁵ Experimentally it is commonly determined that the resolution of these peaks decreases with decreasing oxidation state. These trends are certainly confirmed in the present analysis, which show expected L_{III}-e_g line shapes with respect to crystal structure and Ti oxidation state. The doublet is completely absent in rock salt TiO. Interestingly, for the hetero-nanostructures investigated in this work the line shapes and intensity ratios of the L_{III}-e_g peak in Figure 20b most resemble those of Ti₂O₃.

The peaks labeled *C* and *D*, which originate from excitations of Ti 2*p*_{1/2} core levels into empty Ti 3*d* states, are resolved in Figure 20c. The relative intensities of these peaks as well as their line shapes again most closely resemble those of Ti₂O₃.

This observation of Ti₂O₃-like Ti coordination is reinforced by consideration of the substrate onto which the phase grows, α-Fe₂O₃: trigonal Ti₂O₃ is corundum-type and is therefore isostructural to α-Fe₂O₃. At the thickness considered here, on the order of 1 nm, substrate interactions are expected to play an important role in the evolution of the surface layer. Considering that ALD is a monolayer-by-monolayer growth technique, the Ti₂O₃-like L-edge spectrum is consistent with a crystal growth mechanism (presumably by domain matching epitaxy³²) at the α-Fe₂O₃ surface.

4.4 O K-edge x-ray absorption

Oxygen K-edge absorption spectra, which probe the projected O *p* unoccupied density of states from core *1s* excitations, are presented for Ti_{*x*}O_{*y*}-Fe₂O₃ and reference crystals in Figure 21a. The O *1s* XAS spectra for all samples can be divided into two feature sets of interest: the local intensity maxima between 528 and 535 eV and those positioned at energies greater than 535 eV. The first set of features describe the oxygen 2*p* weight in the transition metal 3*d* band, and for all reference samples contains two peaks related to the t_{2g} and e_g symmetry bands.³³

The conspicuous absence of any observable t_{2g}-e_g splitting for Ti_{*x*}O_{*y*}-Fe₂O₃ requires careful interpretation in light of previous O K-edge XAS studies of transition metal oxide systems.^{33,34} The absence most likely indicates an interfacial charge transfer process, which is expected to be unique to the hetero-nanostructure architecture and its interfacial bonding arrangement. Notably, such phenomena change the occupancy of metal *d* states, which is directly reflected in the *p* unoccupied projected density of states in the presence of *p-d* hybridization. A completely filled t_{2g} orbital will be unavailable for the K-edge transition and will be absent in the O *1s* XAS spectrum. For example, in NiO (nominally *d*⁸ configuration) the 2t_{2g} orbitals are completely occupied, which results in a single sharp feature in this spectral range,^{33,34} similar to that observed for Ti_{*x*}O_{*y*}-Fe₂O₃. This argument is consistent with further analyses of *p-d* hybridization effects, as discussed below.

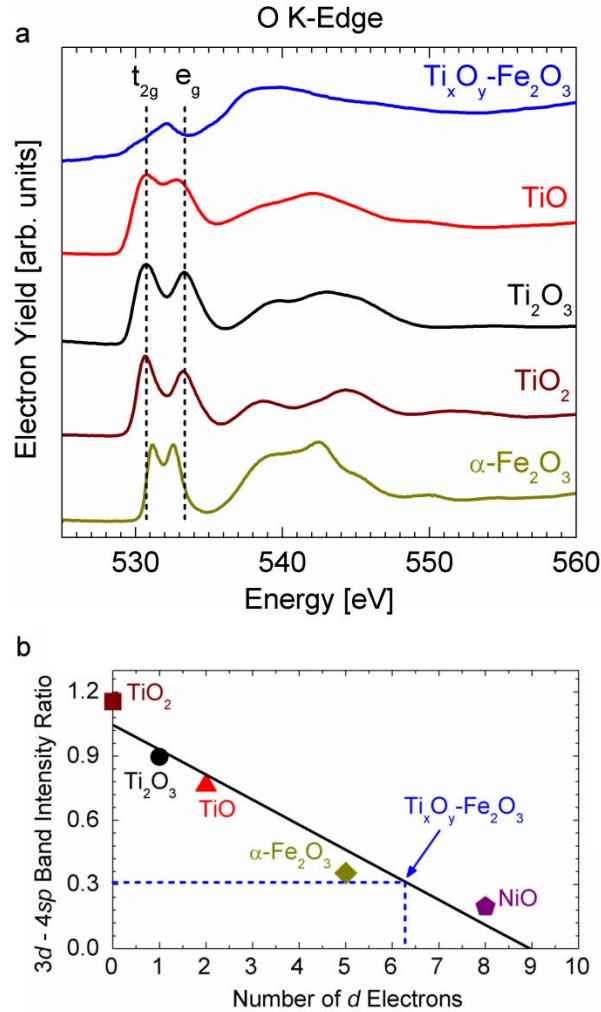


Figure 21. (a) O K_{α} -edge x-ray absorption spectra for $Ti_xO_y-Fe_2O_3$ and reference crystals. Dotted lines indicate the positions of t_{2g} and e_g peak maxima for the TiO_2 reference. (b) The ratios of the integrated areas of the $3d$ bands to those of $4sp$ bands, plotted with respect to number of d electrons in reference crystals. Solid line indicates linear fit to reference data. At d^{10} the linear interpolation does not terminate at 0 because metal $3d$ orbitals shrink in late transition metal oxides, which diminishes experimentally observed $p-d$ hybridization effects.³³

Alternatively, an absence of observable splitting of this peak may relate to size effects and structural distortion present in the hetero-nanostructure. In $\alpha-Fe_2O_3$ nanoparticles for instance, a similar absence was observed and was attributed to large densities of surface states and the presence of strain anisotropy, which results in a distortion of the oxygen site environment.³⁵ These features will tend to broaden the spectral signatures of crystal field splitting.

The features at energies greater than 535 eV are attributable to the hybridization of oxygen p states with metal $4s$ and $4p$ states.³³ The breadth of the spectral range of these features relates to

the covalency of the bonding environment, and the features' line shapes reflect the octahedral symmetry present.³³

The diversity of intensity ratios observed for the two bands ($3d$ and $4sp$ bands) among the materials provides a framework for examining the extent of O p hybridization with the metal d band in the hetero-nanostructure's interfacial region. The importance of such an analysis lies in the relationship between orbital occupancy and the oxygen p character of the transition metal $3d$ band. For example, it is known³³ that the shapes and magnitudes of the $3d$ bands' contribution in oxygen $1s$ XAS spectra are heavily influenced by the presence of a filled e_g orbital in the ground state. This influence divides several defining characteristics of this band between the early- and late-transition-metal oxides.³³ In addition, Reference 33 suggests that a decrease in the relative intensity of the $3d$ band is dominantly caused by a reduction in the number of unoccupied $3d$ states available to mix with O $2p$ states. This suggestion predicts a linear relationship between the bands' intensity ratios and the number of holes. To illustrate this correlation in the present data, the ratios of the integrated areas of the $3d$ bands to those of the $4sp$ bands are plotted with respect to number of $3d$ electrons (Figure 21b). An additional ratio for NiO is included to provide a more complete set of electronic configurations. As expected, a linear relationship is observed among all reference samples. Extrapolation of a linear fit to these data indicates the measured intensity ratio in $Ti_xO_y-Fe_2O_3$ (0.313) corresponds to an intermediate degree of $p-d$ hybridization, greater than that found in d^5 oxides such as $\alpha-Fe_2O_3$, and less than that found in d^8 oxides, such as NiO.³³ These hybridization observations provide additional evidence of the presence of an interfacial charge transfer process within the hetero-nanostructure, which alters the d orbital occupancy and which is reflected in the p unoccupied projected density of states.

4.5 Ti L-edge x-ray emission

The system's occupied electronic structure was probed by x-ray emission spectroscopy (XES). The presence of partially filled $3d$ bands, as discussed above, will be directly evident in L-edge emission spectra.

The Ti $L_{II,III}$ -edge emission spectrum, which for $3d$ transition metals describes the filled portion of the $3d4s$ band, is provided in Figure 22. This figure also includes emission spectra recorded for the reference crystals discussed above, with their respective d electron count indicated. The emission spectrum for stoichiometric TiO_2 , which shows a single intense peak, contrasts considerably with the other recorded spectra. This observation indicates a commonality among the occupied electronic structures of $Ti_xO_y-Fe_2O_3$, TiO , and Ti_2O_3 , the latter two of which are known to possess partially filled Ti $3d$ bands. Reference 25, which is a comprehensive discussion of band structures from emission and absorption spectra of several transition metals and their related compounds, provides an analysis of the $L_{II,III}$ emission spectra for titanium metal as well as six reference oxides of titanium. The peak labeled *A* in Figure 22 is attributed to a transition from the oxygen $2p$ band to a vacancy in the titanium L_{III} shell.²⁵ Peaks *B* and *C*, which are absent in the spectrum for stoichiometric TiO_2 , predominantly represent transitions from occupied $3d$ states (Peak *B*: $Ti\ 3d \rightarrow Ti\ L_{III}$; Peak *C*: $Ti\ 3d \rightarrow Ti\ L_{II}$).²⁵ That these emissions exist in the $Ti_xO_y-Fe_2O_3$ spectrum provides direct confirmation of the presence of Ti $3d$ electrons in the hetero-nanostructure.

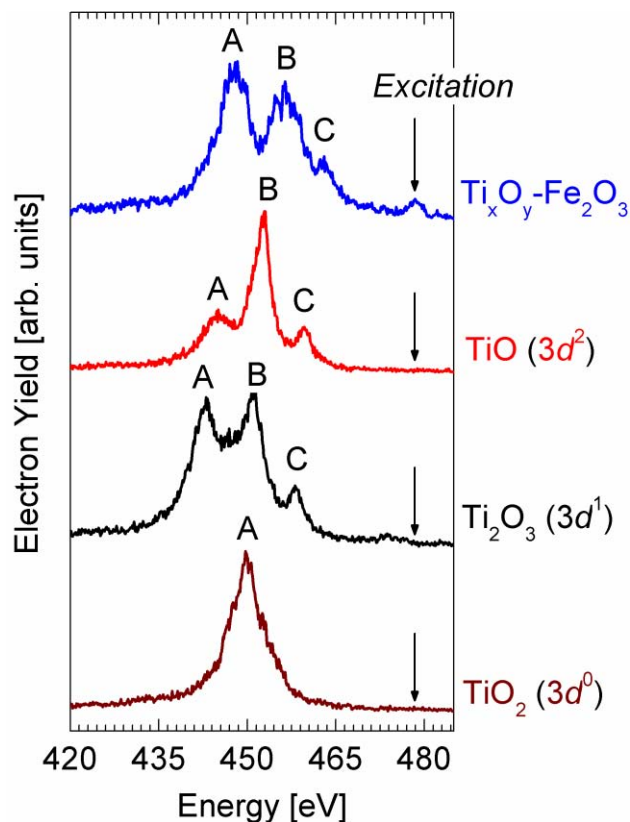


Figure 22. Ti $L_{II,III}$ -edge x-ray emission spectra for $Ti_xO_y-Fe_2O_3$ and reference titania crystals with indicated electronic configurations.

The ability to engineer ultra-thin, electron-rich titanium oxides at low temperatures is of significant technological interest, considering the known macroscopic optical and electronic properties of these materials. TiO , Ti_2O_3 , the Magneli phases³⁶ Ti_4O_7 and Ti_5O_9 , and novel Ti_3O_5 ³⁷, are all electrical conductors, due to their partially filled Ti $3d$ bands.²⁵ These electrical properties manifest in contrast to those of the oxides of heavier $3d$ metals, such as Fe and Ni, which are insulators at room temperature. In $\alpha-Fe_2O_3$ for example, the $3d$ band is exceedingly narrow, which results in a high effective mass and low mobility for electrons.³⁸ In terms of their conduction, electrons in $\alpha-Fe_2O_3$ $3d$ bands are more accurately described as experiencing localized energy levels; in this crystal the $3d$ wave functions do not overlap and remain concentrated near the cation.³⁹ In the lower oxides of titanium, however, the $3d$ wave functions overlap sufficiently to form a conduction band. Ti_2O_3 , whose Ti coordination is most likely mimicked in $Ti_xO_y-Fe_2O_3$, is of particular interest for solar device technologies: the former is semiconducting at room temperature and its presence enhances visible light activity of titania photocatalysts.⁴⁰ It is a conductive oxide⁴¹ and it undergoes a semiconductor-semimetal transition near 120 °C.⁴²

4.6 O 2p orbital analysis

The O K-edge emission spectrum of $Ti_xO_y-Fe_2O_3$ was also studied; these data are plotted directly with absorption data in Figure 23. The energy distances between these features are equal to

corresponding distances in the actual system density of states.²⁵ Examination of the first derivatives of these signals (Figure 23, bottom) provides a quantitative measure of the energy distance between occupied and unoccupied O 2*p* states in the interfacial region of Ti_xO_y-Fe₂O₃. Because the O 2*p* emission spectra red shifts for lower oxides of titanium,²⁵ this energy gap, as defined in the Figure 23, is found to 3.66 eV, greater than that for stoichiometric TiO₂.

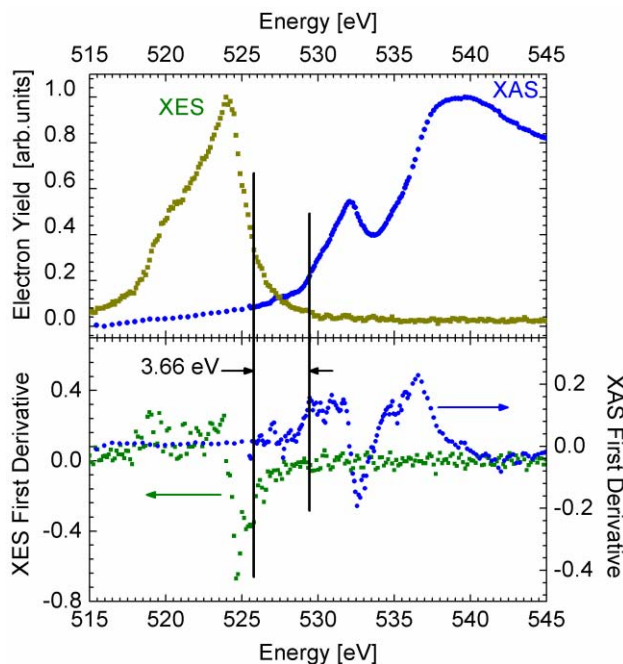


Figure 23. Combined O 1s x-ray emission and absorption spectra for Ti_xO_y-Fe₂O₃, with the first derivatives for each spectrum included for quantification of the energy difference between occupied and unoccupied *p* projected density of states.

4.7 Ultrafast transient absorption spectroscopy

Upon irradiation of α -Fe₂O₃ with energies exceeding the bandgap, free carrier creation and thermalization occurs on extremely fast time scales (< 150 fs;⁴³ < 75 fs⁴⁴). Following this process, ultrafast transient absorption spectroscopy can be used to monitor the subsequent electron relaxation kinetics within the electronic structure of the system.^{43,44,45,46} For this purpose, the Ti_xO_y-Fe₂O₃ was pumped with 540 nm (2.29 eV) 130 fs pulses, and the transient absorbance was collected over a broad range of probe energies. The resultant transient absorbance spectrum, collected 500 fs after excitation, is shown in Figure 24a (absorbance is plotted in terms of change in sample optical density). A spectral transient absorbance signal corresponds to carrier absorption with energy equivalent to the probe photon energy. By measuring these absorptions with time, the recombination dynamics are monitored on picosecond time scales.

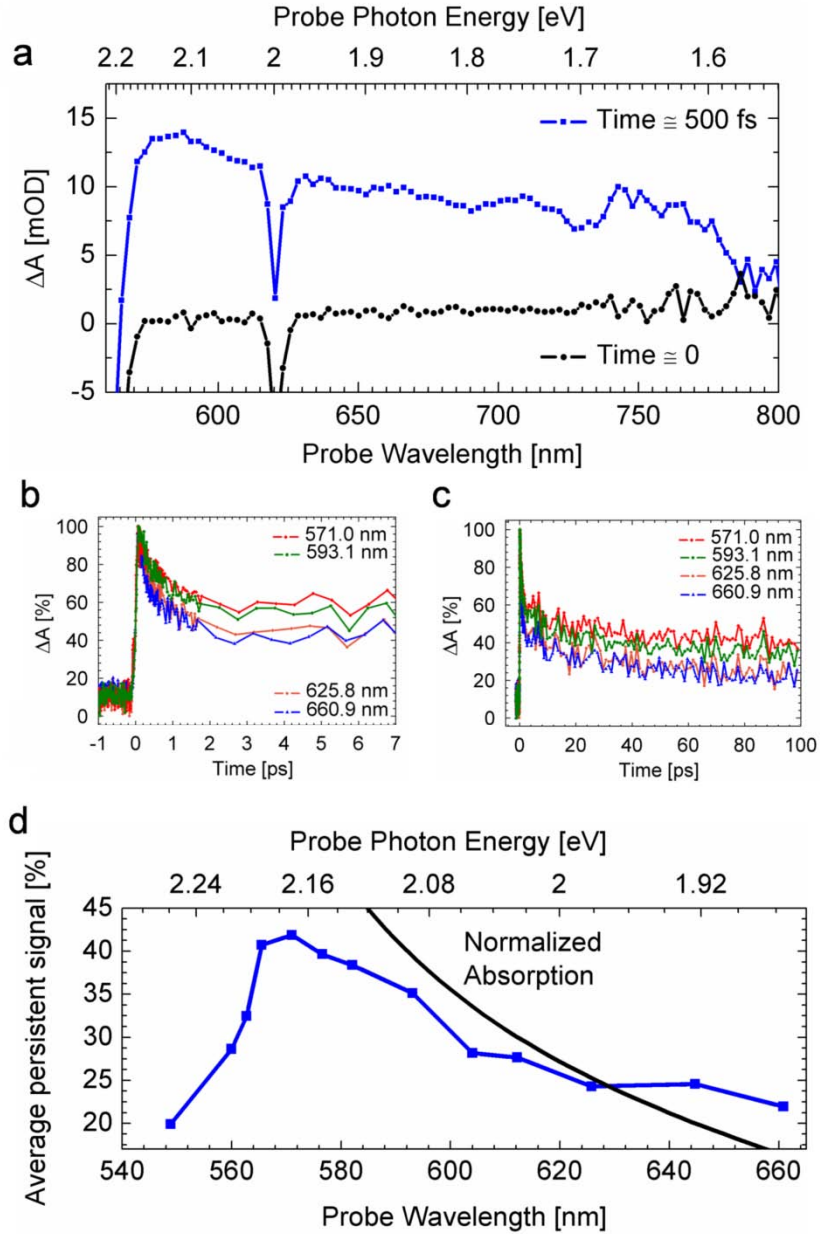


Figure 24. (a) Transient absorbance spectra before (black circles) and 500 fs (blue squares) after excitation. Normalized transient absorption signals for four representative probe wavelengths at ~ 1 ps (b) and ~ 10 ps (c) time regimes. (d) Transient absorption (averages of signals from 70 to 100 ps) after ultrafast excitation of $\text{Ti}_x\text{O}_y\text{-Fe}_2\text{O}_3$ array at various probe wavelengths (blue squares). Also included is the normalized steady-state absorption (black solid line), indicating the correlation of the transient data with the band edge.

Figures 24b and 24c provide the system's normalized absorption transients at two time scales (0-7 ps and 0-100 ps) for representative probe energies. It is evident at ultrafast time scales (Figure 24b) that relaxations from a broad range of states occur via a multiple exponential decay

process. The fast decay component, which is commonly observed in iron oxides,⁴³ occurs within a few ps of the initial relaxation process. The longer component (Figure 24c) has a slower rate and persists to 100 ps and beyond. It is noted that the magnitudes of the decay processes depend on the probe energy, or in other words depend on the energetic position of the corresponding state.

In order to provide a quantitative measure of the spectral differences in decay magnitudes, the persistent absorption signal, defined as the average normalized absorption signal from 70 to 99 ps, was calculated. These values for several probe wavelengths are plotted in Figure 24d. Defined in this way, values of persistent absorption are a measure of the relative lifetimes of excited electrons in states with given energy signatures. It is shown in Figure 24 that the magnitudes of decay of electron relaxation processes depend on the energetic position of such states within the band structure. Interestingly, the maximum transient absorption signal, as averaged over this temporal range, was found to be near 570 nm, which is quite close to the bandgap of α -Fe₂O₃ and the measured band edge of the hetero-nanostructure array. To illustrate this correlation the normalized steady-state optical absorption is also included in Figure 24d (black line).

Previous transient absorption studies of α -Fe₂O₃ have attributed signals over this spectral range to absorption from trapped electrons, for example those electrons captured by surface Fe³⁺ species.^{43,44} This argument is supported by the similar multiple exponential decay kinetics observed for a wide range of probe energies, which suggests these signals share a common physical origin.⁴⁴ Decay from these trap states is primarily nonradiative,⁴³ and is likely mediated by further interaction with lower-lying midgap states. Alternatively, those probe signals whose energies lie near the bandgap of α -Fe₂O₃ may relate to surface-trapped holes. A recent work⁴⁷ assigned transient absorption at 580 nm to holes in α -Fe₂O₃ photoanodes in operating PEC cells, which was corroborated by the utilization of interfacial hole scavenging chemicals.

Despite the context provided by these previous detailed investigations, the confident assignment of transient absorption signals to specific carriers in this material system remains obstructed by the complex nature of the constituent phases. Both phases contain high densities of localized *d* levels, associated with numerous optical transitions in the probed spectral range, as well as high densities of intrinsic and surface defect-induced trap states. Furthermore, the energetics of any previously observed surface trap states in α -Fe₂O₃ are expected to be influenced by the interfacial bonding environment in the hetero-nanostructure system. In addition, the known quantum-confinement effect in the α -Fe₂O₃¹⁹ can potentially cause a spectral shift in the signatures of states electronically active in the relaxation process.

The detailed relationships of the system's carrier dynamics with those of α -Fe₂O₃ and titania crystals will be elucidated in a future investigation. However, this analysis has established the presence of a dense manifold of states, the relaxations from which exhibit multiple exponential decays. Decay magnitudes increase over the temporal range studied when corresponding probe energies deviate from energies near the measured band edge of Ti_xO_y-Fe₂O₃, which suggests there is some relationship between the excited carrier dynamics and the system band structure.

4.8 Conclusions

This report has introduced a new transition metal oxide heterostructure containing junctions of iron oxide (hematite) and titanium oxide nanomaterials, which is readily organized in vertical arrays onto conductive substrates by a combination of inexpensive and scalable techniques. The orbital character of the interfacial region was analyzed by soft x-ray spectroscopies, which indicates the presence of a degree of *p-d* orbital hybridization that is absent from all reference crystals examined. Consideration of spectra relating to the Ti coordination environment suggests a structural relationship is established between the phases. The confirmed existence of Ti 3*d* electrons in the interface suggests the new hetero-nanostructure resulted in spontaneous electron enrichment and thus possesses a unique electronic structure, which likely translates to new emergent electronic properties. These macroscopic system properties are currently under investigation in our laboratories. It is foreseen that this fabrication strategy and the resultant novel materials will open new avenues to engineer the electrical and optical properties of transition metal oxide hetero-nanostructures, to specialize structures for critical applications of oxide electronics, most notably those for solar fuel generation and photovoltaics.

4.9 Experimental methods

4.9.1 Fabrication

The α -Fe₂O₃ nanorod arrays were first fabricated onto SnO₂:F-coated glass (FTO; Pilkington TEC7; 2.3 mm thickness) following the procedure described in reference 19. Ti_xO_y was deposited by ALD at 150 °C using the precursors TiCl₄ and H₂O.⁴⁸ The background flow rate was 80 SCCM N₂, and 15 cycles of Ti_xO_y were deposited with the pulsing sequence 3 s TiCl₄, 60 s N₂ purge, 3 s H₂O, and 60 s N₂ purge. The TiO and Ti₂O₃ reference crystals were commercial powders (TiO: Alfa Aesar, 99.9%; Ti₂O₃: Alfa Aesar 99.8%). Anatase TiO₂ was prepared according to procedures in reference ⁴⁹.

4.9.2 Soft x-ray spectroscopy

X-rays originate from an electronic transition between a localized core state and a valence state. Soft x-ray absorption spectroscopy provides information on the unoccupied electronic structure, and soft x-ray emission spectroscopy provides information on the occupied electronic structure. As a core state is involved, elemental selectivity is obtained because the core levels of different elements are well separated in energy, meaning that the involvement of the inner level makes this probe localized to one specific atomic site around which the electronic structure is reflected as a partial density-of-states contribution. The participation of valence electrons gives the method chemical state sensitivity and further, the dipole nature of the transitions gives particular symmetry information. The x-ray absorption and emission spectroscopy measurements were performed on Beamline 7.0.1 at the Advanced Light Source.

4.9.3 Ultrafast transient absorption spectroscopy

The ultrafast laser system is based on a Quantronix femtosecond laser system,⁵⁰ consisting of an Er-doped fiber oscillator, a regenerative/multi-pass amplifier, and a diode-pumped, Q-switched,

second harmonic Nd:YLF pump laser (527 nm, 10 W capacity). Before injection into the amplifier, chirped pulse amplification is performed to temporally stretch, amplify, and recompress the initial short pulse, resulting in a pulse near its original duration, albeit with a vastly higher energy level (sub-nJ raised to mJ). After amplification, the as-generated fundamental (795 nm) is beam-split to generate both a white light continuum (WLC) probe pulse as well as feeding a tunable optical parametric amplifier (OPA) consisting of two delay stages: a signal pre-amplification stage and a power amplification stage. The output of the OPA was passed through wavelength separators in order to achieve a tunable pump wavelength. The system operates at 750 Hz repetition rate.

The final output was ca. 130 fs pulses centered at 540 nm excitation wavelength which was attenuated with neutral density filters. The pump beam was overlapped spatially and temporally with the WLC probe beam at the sample. The time delay between the pump and probe beams was controlled by a translation stage with 1 μm resolution. Each sample was tested for four cycles to achieve a lower-noise average response.

4.10 References

1. Mannhart, J.; Schlom, *Science* 2010, **327**, 1607-1611.
2. Chakhalian, J.; Freeland, J.W.; Habermeier, H.-U.; Cristiani, G.; Khaliullin, G.; van Veenendaal, M.; Keimer, B. *Science* 2007, **318**, 1114-1117.
3. Zubko, P.; Gariglio, S.; Gabay, M.; Ghosez, P.; Triscone, J.-M. *Annu. Rev. Condense. Matter Phys.* 2011, **2**, 141-165.
4. Nozik, A.J. *Nano Lett.* 2010, **10**, 2735-2741.
5. Vayssieres, L. *On Solar Hydrogen & Nanotechnology*; John Wiley and Sons: Singapore, 2009.
6. Archer, M.D.; Nozik, A.J. *Nanostructured and Photoelectrochemical Systems for Solar Photon Conversion*; Imperial College Press: London, 2008.
7. Atwater, H.A.; and Polman, A. *Nature Mat.* 2010, **9**, 205.
8. Martí, A.; Antolín, E.; Stanley, C.R.; Farmer, C.D.; López, N.; Díaz, P.; Cánovas, E.; Linares, P.G.; Luque, A. *Phys. Rev. Lett.* 2006, **97**, 247701.
9. Grätzel, M. *Inorg. Chem.* 2005, **44**, 6841-6851.
10. Beermann, N.; Vayssieres, L.; Lindquist, S.-E.; Hagfeldt, A. *J. Electrochem. Soc.* 2000, **147**, 2456-2461.

11. Snaith, H.J.; Ducati, C. *Nano Lett.* 2010, **10**, 1259-1265.
12. Zhong, H.; Zhou, Y.; Yang, Y.; Yang, C.; Li, Y. *J. Phys. Chem. C* 2007, **111**, 6538-6543.
13. Zhang, J.; Tang, Y.; Lee, K.; Ouyang, M. *Nature* 2010, **466**, 91-95.
14. Walter, M.G.; Warren, E.L.; McKone, J.R.; Boettcher, S.W.; Mi, Q.; Santori, E.A.; Lewis, N.S. *Chem. Rev.* 2010, **110**, 6446-6473.
15. Vayssieres, L.; Hagfeldt, A.; Lindquist, S.-E. *Pure Appl. Chem.* 2000, **72**, 47-52.
16. Puurunen, R.L. *J. Appl. Phys.* 2005, **97**, 121301-121352.
17. Bakke, J.R.; Jung, H.J.; Tanskanen, J.T.; Sinclair, R.; Bent, S.F. *Chem. Mater.* 2010, **22**, 4669-4678.
18. Vayssieres, L.; Beermann, N.; Lindquist, S.-E.; Hagfeldt, A. *Chem. Mater.* 2001, **13**, 233-235.
19. Vayssieres, L.; Sathe, C.; Butorin, S.M.; Shuh, D.K.; Nordgren, J.; Guo, J.. *Adv. Mater.* 2005, **17**, 2320-2323.
20. Liou, F.-T.; Yang, C.Y.; Levine, S.N. *J. Electrochem. Soc.* 1982, **129**, 342-345.
21. Peng, L.; Xie, T.; Lu, Y.; Fan, H.; Wang, D. *Phys. Chem. Chem. Phys.* 2010, **12**, 8033-8041.
22. Mohapatra, S.K.; Banerjee, S.; Misra, M. *Nanotechnology* 2008, **19**, 315601.
23. Guo, J. *Int. J. Quantum Chem.* 2009, **109**, 2714-2721.
24. Biener, J.; Bäumer, M.; Wang, J.; Madix, R.J. *Surface Science* 2000, **450**, 12-26.
25. Fischer, D.W.; Baun, W.L. *J. Appl. Phys.* 1968, **39**, 4757-4776.
26. de Groot, F.M.F.; Figueiredo, M.O.; Basto, M.J.; Abbate, M.; Petersen, H.; Fuggle, J.C. *Phys. Chem. Minerals* 1992, **19**, 140-147.
27. Thomas, A.G.; [Flavell](#), W.R.; [Mallick](#), A.K.; [Kumarasinghe](#), A.R.; [Tsoutsou](#), D.; [Khan](#), N.; [Chatwin](#), C.; [Rayner](#), S.; [Smith](#), G.C. *Phys. Rev. B* 2007, **75**, 035105.
28. Chen, X.; Glans, P.-A.; Qiu, X.; Dayal, S.; Jennings, W.D.; Smith, K.E.; Burda, C.; Guo, J. *J. of Electron Spectroscopy and Related Phenomena* 2008, **162**, 67-73.

29. de Groot, F.M.F.; Fuggle, J.C.; Thole, B.T.; Sawatzky, G.A. *Phys. Rev. B* 1990, **41**, 928.
30. Lusvardi, V.S.; Barteau, M.A.; Chen, J.G.; Eng Jr., J.; Fruhberger, B.; Teplyakov, A. *Surface Science* 1998, **397**, 237-250.
31. Crocombette, J.P.; Jollet, F. *J. Phys.: Condens. Matter* 1994, **6**, 10811-10821.
32. Narayan, J.; Larson, B.C. *J. Appl. Phys.* 2003, **93**, 278-285.
33. de Groot, F.M.F.; Grioni, M.; Fuggle, J.C.; Ghijsen, J.; Sawatzky, G.A.; Petersen, H. *Phys. Rev. B* 1989, **40**, 5715-5723.
34. Chen, J.G. *Surf. Science Reports* 1997, **30** 1-152.
35. Park, T.-J.; Sambasivan, S.; Fischer, D.A.; Yoon, W.-S.; Misewich, J.A.; Wong, S.S. *J. Phys. Chem. C* 2008, **112**, 10359-10369.
36. Andersson, S.; Collén, B.; Kuylenstierna, U.; and Magnéli, A. *Acta Chemica Scandinavica* 1957, **11**, 1641-1652.
37. Ohkoshi, S.-i.; Tsunobuchi, Y.; Matsuda, T.; Hashimoto, K.; Namai, A.; Hakoe, F.; Tokoro, H. *Nature Chem.* 2010, **2**, 539-545.
38. Morin, F.J. *Phys. Rev.* 1954, **93**, 1195.
39. Morin, F.J. *Bell System Tech. J.* 1958, **37**, 1047-1084.
40. Liu, H.; Yang, W.; Ma, Y.; and Yao, J. *Appl. Catal. A: General* 2006, **299**, 218-223.
41. Honig, J.M.; and Reed, T.B. *Phys. Rev.* 1968, **174**, 1020-1026.
42. Honig, J.M. *Rev. Modern Phys.* 1968, **40**, 748-751.
43. Cherepy, N.J.; Liston, D.B.; Lovejoy, J.A.; Deng, H.; Zhang, J.Z. *J. Phys. Chem. B* 1998, **102**, 770-776.
44. Nadtochenko, V.A.; *Russian Chem. Bulletin, International Edition* 2002, **51**, 457-461.
45. Joly, A.G.; Williams, J. R.; Chambers, S. A.; Xiong, G.; Hess, W.P.; Laman, D.M. *J. Appl. Phys.* 2006, **99**, 053521.
46. He, Y.P.; Miao, Y.M.; Li, C.R.; Wang, S.Q.; Cao, L.; Xie, S.S.; Yang, G.Z.; Zou, B.S.; Burda, C. *Phys. Rev. B* 2005, **71**, 125411.

47. Pendlebury, S.R.; Barroso, M.; Cowan, A.J.; Sivula, K.; Tang, J.; Grätzel, M.; Klug, D.; Durrant, J.R. *Chem. Commun.* 2011, **47**, 716-718.
48. Ardalan, R.; Brennan, T.B.; Lee, H.B.R.; Bakke, J.R.; Ding, I.K.; McGehee, M.D.; Bent, S.F. *ACS Nano* 2011, **5**, 2834-2860.
49. Mattsson, A.; Leideborg, M.; Larsson, K.; Westin, G.; Österlund, L. *J. Phys. Chem. B* 2006, **110**, 1210-1220.
50. Newhouse, R.J.; Wang, H.; Hensel, J.K.; Wheeler, D.A.; Zou, S.; Zhang, J.Z. *J. Phys. Chem. Lett.* 2011, **2**, 228-235.

Appendix: Research Publications

1. **C.X. Kronawitter**, Z.X. Ma, D. Liu, S.S. Mao, B.R. Antoun, Engineering impurity distributions in photoelectrodes for solar water oxidation, *Adv. Energy Mater.*, 2011, *Published, In Press.*.
2. **C.X. Kronawitter**, L. Vayssieres, S. Shen, L. Guo, D.A. Wheeler, J.Z. Zhang, B.R. Antoun, S.S. Mao, A perspective on solar-driven water splitting with all-oxide hetero-nanostructures, *Energy Environ. Sci.*, **2011**, *4*, **3889**.
3. **C.X. Kronawitter**, J.R. Bakke, D.A. Wheeler, W.-C. Wang, C. Chang, B.R. Antoun, J.Z. Zhang, J. Guo, S.F. Bent, S.S. Mao, L. Vayssieres, Electron enrichment in 3d transition metal oxide hetero-nanostructures, *Nano Lett.*, **2011**, *11*, 3855.
4. **C.X. Kronawitter**, S.S. Mao, B.R. Antoun, Doped, porous iron oxide films and their optical functions and anodic photocurrents for solar water splitting, *Appl. Phys. Lett.*, **2011**, *98*, 092108.

International conference presentations

- Materials Research Society Fall Meeting 2011, Oral presentation: **C.X. Kronawitter**, L. Vayssieres, B.R. Antoun S.S. Mao, Metal oxide hetero-nanostructure arrays for solar water oxidation, *Symposium Z: Functional Metal-Oxide Nanostructures*, November 28 2011, Boston, MA, USA (Accepted).
- Materials Research Society Spring Meeting 2010, Invited talk and Session Chair: **C.X. Kronawitter**, S.S. Mao, B.R. Antoun, Metal oxide films and nanostructures for solar energy conversion, *Symposium N: Functional Oxide Nanostructures and Heterostructures*, April 7 **2010**, San Francisco, CA, USA.
- SPIE Optics and Photonics, Oral presentation: **C.X. Kronawitter**, S.S. Mao, B.R. Antoun, Pulsed laser deposition of metal oxide photoelectrodes for solar-driven hydrogen production, *Conference 7408: Solar Hydrogen and Nanotechnology IV*, August 3 **2009**, San Diego, CA, USA.

Seminars

- Sandia National Laboratories Technical Seminar, **C.X. Kronawitter**, S.S. Mao, B.R. Antoun, Metal oxide films and nanomaterials for solar water oxidation, February 2 **2011**, Livermore, CA, USA.
- Sandia National Laboratories Technical Seminar, **C.X. Kronawitter**, S.S. Mao, B.R. Antoun, Experimental considerations for preparation of thin film semiconductor photocatalysts by pulsed laser deposition, May 7 **2008**, Livermore, CA, USA.

Distribution

Electronic Distribution

1	Prof. S. Mao		
	Lawrence Berkeley National Laboratory		
	1 Cyclotron Road, MS 70-108B		
	Berkeley, CA 94720		
1	Coleman Kronawitter		
	Lawrence Berkeley National Laboratory		
	1 Cyclotron Road, MS 70-108B		
	Berkeley, CA 94720		
1	MS9004	P. B. Davies	08100
1	MS9153	R. G. Miller	08200
1	MS0942	M.E. Gonzales	08240
1	MS9403	A. Vance	08223
1	MS9042	C. D. Moen	08256
1	MS0942	B. R. Antoun	08256
1	MS9042	M. L. Chiesa	08259
1	MS9054	R. W. Carling	08300
1	MS9052	D. E. Dedrick	08367
1	MS9405	G. D. Kubiak	08600
1	MS9291	B. Simmons	08630
1	MS1349	J. E. Miller	01815
1	MS0359	Donna L. Chavez	01911
1	MS9018	Central Technical Files	08944
1	MS0899	RIM-Reports Management	09532

